Environmental Science & Technology

pubs.acs.org/est

Article

Self-Perpetuating Carbon Foam Microwave Plasma Conversion of Hydrocarbon Wastes into Useful Fuels and Chemicals

Guiyin Xu, Haibin Jiang, Myles Stapelberg, Jiawei Zhou, Mengyang Liu, Qing-Jie Li, Yunteng Cao, Rui Gao, Minggang Cai, Jinliang Qiao,* Mitchell S Galanek, Weiwei Fan, Weijiang Xue, Benedetto Marelli, Meifang Zhu,* and Ju Li*

Cite This: *Environ. Sci. Technol.* 2021, 55, 6239−6247

Read Online

ABSTRACT: White wastes (unseparated plastics, face masks, textiles, etc.) pose a serious challenge to sustainable human development and the ecosystem and have recently been exacerbated due to the surge in plastic usage and medical wastes from COVID-19. Current recycling methods such as chemical recycling, mechanical recycling, and incineration require either pre-sorting and washing or releasing CO_2. In this work, a carbon foam microwave plasma process is developed, utilizing plasma discharge to generate surface temperatures exceeding ∼3000 K in a N_2 atmosphere, to convert unsorted white wastes into gases (H_2, CO, C_2H_4, C_3H_6, CH_4, etc.) and small amounts of inorganic minerals and solid carbon, which can be buried as artificial "coal". This process is self-perpetuating, as the new solid carbon asperities grafted onto the foam's surface actually increase the plasma discharge efficiency over time. This process has been characterized by *in situ* optical probes and infrared sensors and optimized to handle most of the forms of white waste without the need for pre-sorting or washing. Thermal measurement and modeling show that in a flowing reactor, the device can achieve locally extremely high temperatures, but the container wall will still be cold and can be made with cheap materials, and thus, a miniaturized waste incinerator is possible that also takes advantage of intermittent renewable electricity.

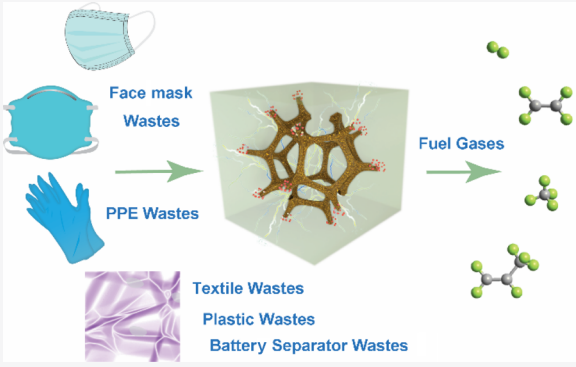

White wastes are ubiquitous, ranging from food packaging to used face masks/textiles, to electronic device components such as battery separators, and more (Figure S1). Unfortunately, the production of white wastes is increasing, with little hope to reach a global "peak waste" production before 2100.[1] Disposal of white wastes is becoming a pressing issue with several of the world's largest landfills already beginning to reach their limits. The COVID-19 pandemic has only exacerbated the problem, by increasing the reliance on plastic goods and personal protective equipment (PPE) to contain the spread of the virus.[2,3] Poorly stored and littered white wastes can be easily transported into the ocean by wind and rain. For example, 8 million metric tons of plastic enters the ocean every year and poses a grave threat to marine life.[4] These long-lasting debris take up to 500 years to biodegrade in the ocean.[5] Microplastics formed by weathering and biodegradation are often detected in estuaries, lakes, coastal waters, and beaches (Table S1)[6,7] and could also be found in deep-sea sediments, ice cores, and polar waters (Figure S2).[6,8−11]

The current recycling methods used are mechanical and chemical recycling, with both methods limited to processing only polyethylene and poly(ethylene terephthalate) at an industrial scale.[12,13] Chemical recycling also requires sorting processes to separate white wastes into pure feedstocks.[14] Furthermore, catalysts limit the efficiency and selectivity of chemical recycling. These processes call for large capital equipment and centralized processing plants, and transportation of distributed white wastes to these large plants incurs additional costs. A local community level treatment of white wastes that does not require mechanical sorting and takes advantage of intermittent renewable electricity would be highly desirable.[15,16]

White wastes are mostly long-chain hydrocarbons and in a reducing atmosphere at high temperatures will decompose into H_2, CO, C_2H_4, C_3H_6, CH_4, etc. These gases plus residual solid carbon, C_n, are valuable ingredients for the chemical industry, acting as feedstock to make fresh plastics and other useful chemicals. It is essential that solid carbon C_n components are not oxidized in the process, as that would produce unwanted CO_2 emission. This residual carbon should also be well contained, as

Received: October 16, 2020
Revised: March 21, 2021
Accepted: March 22, 2021
Published: April 6, 2021

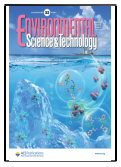

https://doi.org/10.1021/acs.est.0c06977
Environ. Sci. Technol. 2021, 55, 6239−6247

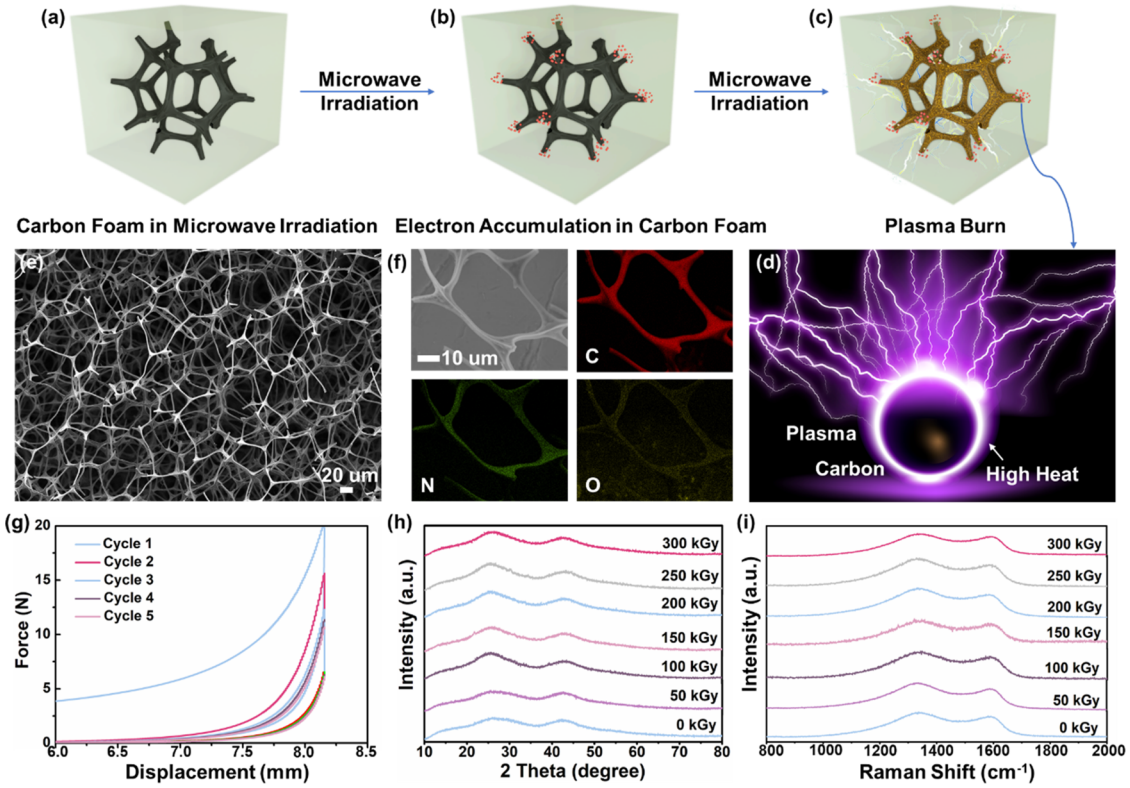

Figure 1. (a−d) Schematic illustration of plasma ignition and heat production by the carbon foam during microwave irradiation. (e) Scanning electron microscopy (SEM) image of the carbon foam. (f) Scanning transmission electronic microscope (STEM) image of the carbon foam and the corresponding elemental mapping images for carbon, nitrogen, and oxygen. (g) Cyclic stress−strain curves of the carbon foam. (h) X-ray diffraction (XRD) patterns and (i) Raman spectrum of the carbon foam irradiated at different kGy doses (0, 50, 100, 150, 200, 250, and 300 dose).

it would become another source of pollution in the form of soot, as in the case of careless incineration. Finally, inorganic components such as dyes or fillers, like SiO_2 and Al_2O_3, are unavoidable in real waste and must be collected as compact solid waste. With standard incineration, not only CO_2 greenhouse gases are generated using conventional incineration practices, but unavoidable inorganic residue area may also become airborne particulates and contribute to PM 2.5 pollution. The optimal recycling process should thus be

$$\text{Unsorted white wastes} \rightarrow H_2, CO, C_2H_4, C_3H_6, CH_4, \text{etc. gases} + \text{coal-like minerals} \quad (1)$$

converting waste into gaseous feedstock and stable coal-like solids. This would allow for the disposal of the $C_n/SiO_2/Al_2O_3/$... coal composites underground, such as an abandoned coal mine. However, special attention must be made to ensure that these residual solids do not leach into ground water. The gases collected (e.g., H_2) may be utilized in fuel cells or be sent to chemical factories (e.g., C_2H_4) *via* gas pipelines to synthesize new plastics and chemicals, thus closing the materials loop, without stressing the road transportation network.

The standard approach to (1) requires large industrial installations and pressure vessels made from expensive alloys due to the uniformly high temperatures and pressures involved. This work proposes the use of microwave plasma discharge, where the local temperature can reach several thousand Kelvins due to the generation of microplasmas on the surface of the catalyst while maintaining manageable temperatures within the reactor chamber. This alternative method could forego expensive pressure vessels and instead rely upon cheaper materials such as those found in household microwave ovens. Microwave ovens create standing-wave electromagnetic radiation in the frequency range of 300 MHz to 300 GHz.[17] Due to itinerant electrons in the carbon foam and incident microwaves, a large electric field can form on the surface of the foam, inducing gas plasma discharge, ionizing nearby N_2 gas and generating local temperatures in excess of 3000 K.

Research in microwave-assisted plasmas for waste processing is relatively new and has recently focused on designing new catalysts to more readily ionize plasmas. State-of-the-art techniques utilize metals like tungsten (W), copper (Cu), or iron (Fe) as electrodes or catalysts to induce plasma discharge.[18] Graphitic or activated carbon may be cheaper alternatives and provide advantages with their ability to readily absorb microwaves and withstand high temperatures prior to sublimation.[19,20] Several recent examples are included in Table S2 to highlight the multiple use cases of microwave-assisted plasma discharge in processing waste, ranging from electronics to natural gases and oils, to plastics, and even baby diapers. This wide range in applications highlights the flexibility of microwave-assisted plasma chemistry, minimizing the need for pre-processes and more importantly removing the need for pre-sorting.

Herein, a carbon foam microwave plasma (CFMP) process was developed to generate high local temperatures to transform white wastes into hydrogen gas and useful chemicals like ethylene (C_2H_4), propylene (C_3H_6), and methane (CH_4). While plasmas can promote various kinds of chemical reactions by creating free radicals, ions, and high temperatures in ambient conditions, the process to form plasma discharge is not

https://doi.org/10.1021/acs.est.0c06977
Environ. Sci. Technol. 2021, 55, 6239−6247

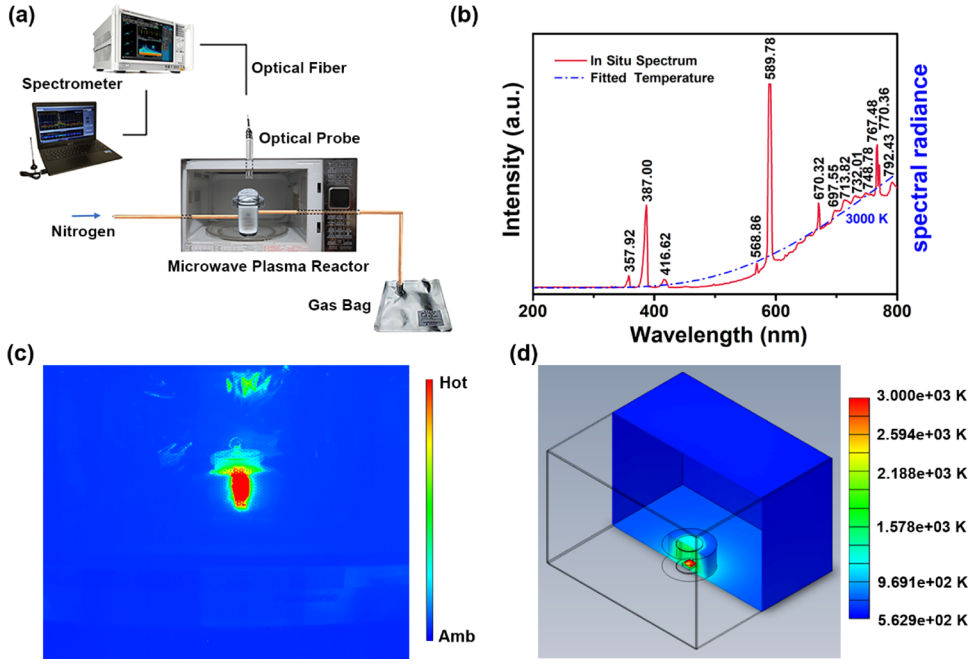

Figure 2. (a) Schematic illustration of the *in situ* spectrum measurement system for the microwave plasma reactor. (b) *In situ* spectrum and fitted temperature of carbon foam in microwave irradiation. (c) *In situ* temperature distribution of the microwave plasma reactor by a forward-looking infrared camera. The linear color scale represents the ambient and hot temperature. Absolute values of temperature are not reported due to the existence of the microwave oven door in the viewing direction. (d) Steady-state thermal analysis simulated with SolidWorks 2020.

straightforward.[21−26] In this work, it is shown that exposing an appropriately designed carbon foam to nitrogen gas and microwaves can induce plasma discharging, forming nitrogen plasma. During this short and localized energy burst, plasmas decompose the white wastes into H-bearing small gas molecules, with excess high-quality graphitic carbon precipitating out as solid C_n grafted onto the pre-existing foam, forming a self-perpetuating "carbon foam cycle". A small amount of CO could also be generated due to trace amounts of oxygen in the atmosphere and oxygen from the original polymer. Surprisingly, C_n is deposited on the surface of the carbon foam, forming electrically conductive barbed tips that facilitate further discharge, so much so that efficiency of the foam increases over time.

■ EXPERIMENTAL SETUP

In this work, a carbon foam was used to induce plasma discharge with microwave irradiation (Figure 1a−d). The carbon foam was initially produced by the thermal decomposition of commercial melamine foams in nitrogen, with yield up to 60 wt % (Figure S3). A distinct weight loss from ∼400 °C is shown in the thermal gravimetric (TG) curve, corresponding to the escape of H and C atoms from melamine.[27] The TG weight curve stabilized after 900 °C, indicating that a complete transformation of melamine to carbon had occurred. Carbon foam has a structure akin to a three-dimensional barbed pentagonal honeycomb (Figure 1e and Figure S4a,b). Due to the removal of H and C atoms from melamine, the surface of the carbon foam was porous (Figure S4c). High-resolution transmission electron microscopy (HRTEM) images show abundant micropores and mesopores within the foam (Figure S4d), measuring a Brunauer−Emmett−Teller (BET) surface area of 36.32 m^2 g^{-1}, a pore volume of 0.06 cm^3 g^{-1}, and an average pore size of 6.15 nm (Table S3).

X-ray photoelectron spectroscopy (XPS) and scanning transmission electron microscopy (STEM) results verify a uniform distribution of carbon, nitrogen, and oxygen in the carbon foam (Figure 1f and Figure S5).[28,29] The apparent bulk electrical conductivity of the carbon foam is ∼3 S m^{-1}, which considering its high porosity (nominal density is ∼5 mg cm^{-3}, and thus, porosity is ∼99.6 vol %) suggests a very high electric conductivity at the microscopic level. Moreover, the carbon foam also demonstrates sufficient mechanical properties (Figure 1g and Video S1). Even under extreme conditions, such as exposure to gamma-ray irradiation (50−300 kGy), the carbon foam structure remained stable, and its physical surface properties showed minimal changes (Figures S6−S13 and Table S3). X-ray diffraction (XRD) patterns are shown in Figure 1h, where the two broad signals around 26 and 44° correspond to the (002) and (100) spacings of the graphene sheets, respectively. For the first peak at 26°, the intensity remained unchanged after 50 kGy of gamma irradiation. After 100 kGy, the intensity of the peak increased slightly but then remained constant after exposure to 150, 200, 250, and 300 kGy. The peak at 44° showed nominal changes in intensity after exposure to gamma irradiation. The Raman spectra in Figure 1i show two strong bands at ∼1590 and 1330 cm^{-1}, corresponding to the G-band and the disorder-induced D-band. There are few changes of these peaks after the carbon foam is exposed to gamma irradiation.

The carbon foam utilizes plasma discharging to generate high local temperatures within the microwave oven. The process is as follows: After the carbon foam absorbs incident microwaves, electrons/holes accumulate at the asperities of the carbon foam (Figure 1b). With the accumulation of free electrons, high local electrical fields are then generated. Next, the accumulated electrons begin to emit into free space as cathodic ray emissions, and these electrons ionize the nitrogen gas, which set off a cascade of charged-particle ionizations, accelerations, and

https://doi.org/10.1021/acs.est.0c06977
Environ. Sci. Technol. 2021, 55, 6239−6247

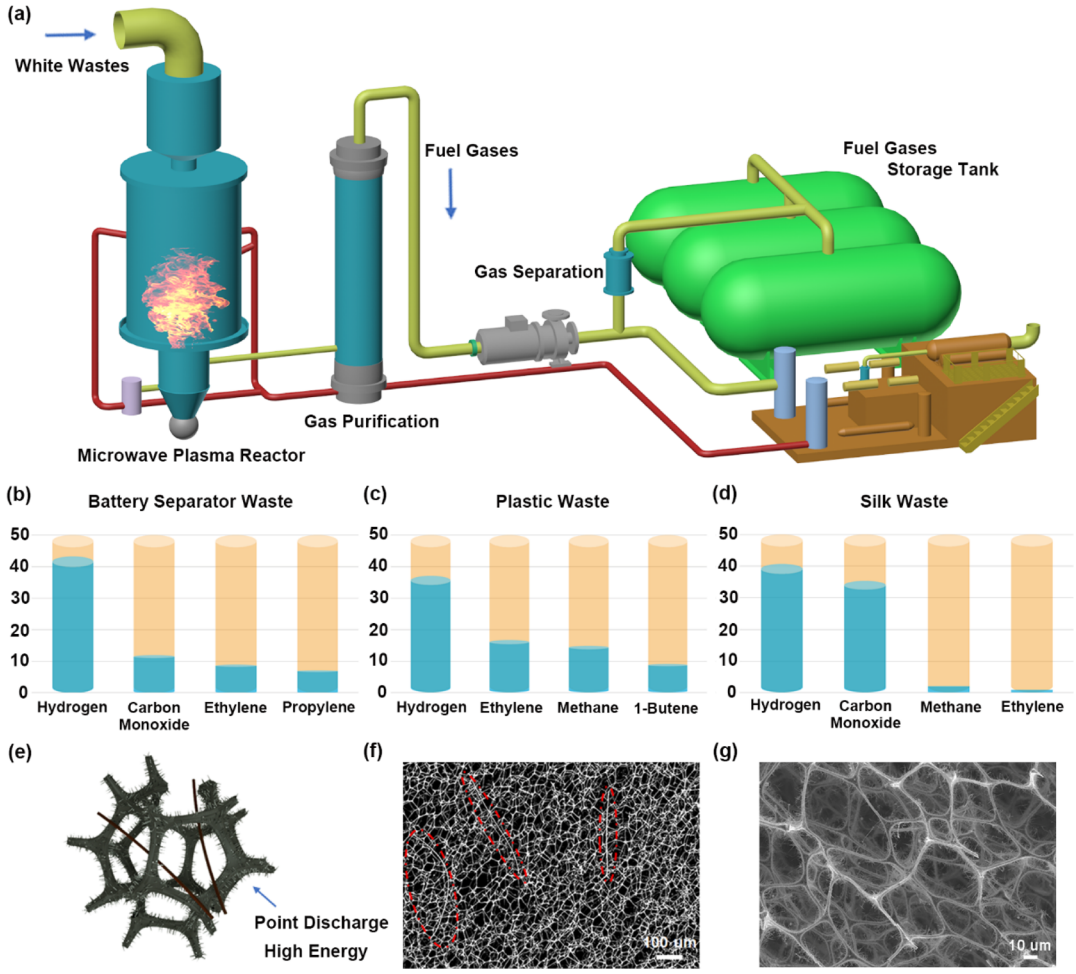

Figure 3. (a) Diagram of the industrial process for the white waste treatment by carbon foam microwave plasma. Main gas composition (vol %) of (b) plastic waste, (c) battery separator waste, and (d) silk waste by the carbon foam and microwave irradiation. A more detailed gas composition is shown in Table S5. (e) Schematic diagram of the carbon foam after microwave irradiation for the battery separator waste treatment. (f,g) Scanning electron microscopy (SEM) images of the carbon foam with battery separator waste after microwave irradiation of 330 W and 8 s.

collisions under the electric field. Once plasma discharging occurs, plasma is formed (Figure 1c), resulting in high temperatures on the surface of carbon foam (Figure 1d) and sending out bright lights (see Videos S2−S8).

Due to the high heating rates and temperatures involved in this nitrogen microwave plasma process, it is not easy to measure the reaction temperature. An *in situ* spectral measurement system was used to indirectly estimate the temperature (Figure 2a). The peaks on this spectrum radiance plot correspond to the electronic transitions between the different energy levels in the carbon foam and nitrogen gas (Figure 2b).[30] The peaks at 387.00 and 589.78 nm correspond to the transitions of $2s^22p4p$ to $2s2p^2(^4P)3p$ and $2s2p^2(^4P)3s$ to $2s2p^2(^4P)3p$ in nitrogen, respectively (Table S4). The peak located at 357.92 nm is attributed to the transition of $2s2p(^3P^\circ)3p$ to $2s2p(^3P^\circ)4s$ in carbon. The high lattice energy in the solid phase shows that the peak intensity of nitrogen is higher than that of carbon. Overall, the spectrum radiance complies well with the Planck's law of black-body radiation[31]

$$B_\nu(T) = \frac{2h\nu^3}{c^2}\frac{1}{e^{h\nu/kT} - 1} \tag{2}$$

where ν is the frequency of electromagnetic radiation; $B_\nu(T)$ is the spectral radiance density of frequency ν radiation; T is the absolute temperature of the body; h is the Planck constant; c is the speed of light in a vacuum; k is the Boltzmann constant. By proper scaling and least-square regression on the measured spectrum radiance, we estimate that the microwave plasma process generates a temperature of 3000 K in a few seconds. The local high temperature enables the decomposition of even very stable organic wastes. The local high temperature was recorded by an *in situ* infrared (IR) sensor (Figure 2c, Figure S14, and Video S2). During the process, a high temperature region localized around the sample surface (at the center of the microwave plasma reactor) is observed after a few seconds. This suggests that the surface of the carbon foam, when exposed to the microwave plasma process, can serve as an effective medium for waste pyrolysis. Since high local temperatures are generated, ceramic fiber blankets were used to insulate the CFMP system (Figure S15a,b and Video S3). While a decrease in thermal emission from the microwave oven door limits our capability to quantify absolute temperature scales, it is clear that highly localized heat zones are generated on the carbon foam surface.

Thermal analysis on the microwave reactor designed in this work was done to understand temperature profiles during steady-state operation, as an industrial system would likely be designed to run continuously to maximize productivity. The thermal analysis was done using SolidWorks Simulation, which

https://doi.org/10.1021/acs.est.0c06977
Environ. Sci. Technol. 2021, 55, 6239−6247

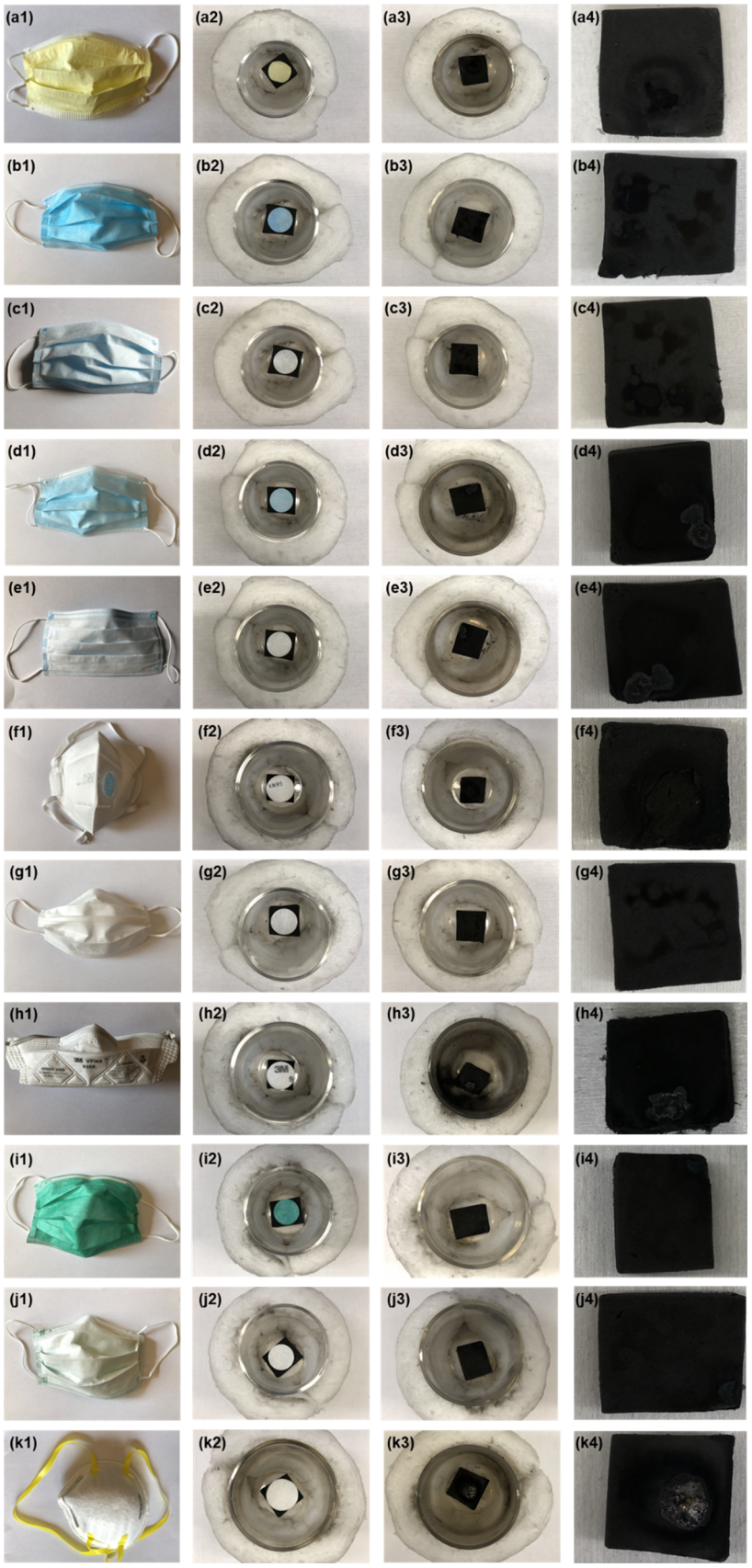

Figure 4. Digital images of mask wastes (a1−k1) and mask wastes on the carbon foam (a2−k2) before and (a3−k3 and a4−k4) after microwave irradiation.

https://doi.org/10.1021/acs.est.0c06977
Environ. Sci. Technol. 2021, 55, 6239−6247

employs the Stefan−Boltzmann equation for radiation heat transfer at a steady state.

$$q = \epsilon\sigma A T^4 \tag{3}$$

where ϵ is the emissivity of an object, σ is the Stefan−Boltzmann constant, A is the area of the object radiating heat, and T is the temperature of the object. SolidWorks makes the distinction between surface to surface and surface to ambient radiative heat transfer by introducing a view factor term, F, into eq 3. This view factor is calculated based on meshing and user input and ranges from 0 to 1.

Figure 2d and Figure S16a show the side and top cutouts of the thermal analysis with a temperature bar showing the absolute temperatures within the system. This simulation is run at a steady state and acts as an overestimate for the prototype environment tested in this work. The thermal insulation does an adequate job of containing the extreme temperatures generated by the carbon foam while also maintaining an environment hot enough within the beaker to pyrolyze the plastics nearby in an autocatalyzing manner. Figure S16b and Figure S16c show the side and top down profiles as well but do so by cutting the system in half at the Z and Y axes, respectively. The side profile shows the temperature distribution for the system when run continuously, giving insights into what the maximum temperatures would be during operation. In the top-view cutout, the bottom panel of the microwave would experience temperatures exceeding 800 K due to the lack of convective heat transfer enacting on that panel, as the microwave is assumed to be placed on a table. This could be rectified by placing a ceramic fiber blanket under the quartz container or by increasing gas flow to the bottom panel and raising the microwave several inches off its table. Implementing these small fixes could enable the safe, continuous operation of the CFMP, without relying on expensive high-temperature vessels and complicated thermal management systems.

RESULTS AND DISCUSSION

The number of steps taken from white wastes to recycled industrial materials is drastically pared down with the CFMP process. White wastes are first cut into pieces to expose more surface area to plasma and enhance the overall energy utilization of the system (Figure 3a).[32,33] The broken-down wastes are then transferred into the microwave plasma reactor to be pyrolyzed into gases (H_2, CO, etc.) and then separated into different storage tanks according to their chemical composition and boiling points.[34] Hydrogen-carbon monoxide products can then be directly fed into the Fischer−Tropsch process to synthesize chemical products.[35]

In addition to plastics and silks, the fast development of lithium-ion batteries for electric vehicles and grid-scale energy storage[36,37] has necessitated the accommodation of battery separators in the CFMP process. To recycle this more complicated class of waste, the CFMP reactor was used to pyrolyze the multicomponent separator polymers without pre-sorting. The output power of the microwave and the reaction time are discussed in the Supporting Information, Figures S17−S21. For all experiments, a subsecond intermittence period of no microwaves was present due to the design of our consumer microwave oven. A reaction time of 8 s was selected with varying output powers (110, 220, and 330 W) for our initial experiments. At 110 W (Video S4), the battery separator waste only shrank on the surface of the carbon foam (Figure S17a−c). At 220 W (Video S5), residual amounts of battery separator waste remained (Figure S18a−c). However, at 330 W (Video S6), the surface of the carbon foam was clean (Figure S19a−c). After establishing the optimal output power (330 W), multiple reaction times (4, 8, and 12 s) were tested. After 4 s (Video S7 and Figure S20a−c), the result was similar to the 220 W, 8 s trial and showed an insufficient treatment of the battery waste. At 12 s (Video S8 and Figure S21a−c), an experimental result similar to 330 W, 8 s was observed.

In addition to battery separators, plastics, and silks, different types of face masks were successfully treated by CFMP (Figure 4), demonstrating a promising recycling method of handling the surge in medical wastes due to COVID-19. About 1.2 wt % solid carbon residue was left after the CFMP process compared to the initial white waste.

Gases obtained from white wastes using CFMP were analyzed with gas chromatography−mass spectrometry (GC−MS). Battery separator wastes yielded the following: 43.31 vol % hydrogen gas, 11.88 vol % carbon monoxide, 8.86 vol % ethylene, 7.10 vol % propylene, and 4.50 vol % methane (Figure 3b and Table S5). Plastic wastes yielded 37.07 vol % hydrogen gas, 16.58 vol % ethylene, 14.89 vol % methane, 8.99 vol % 1-butene, 5.85 vol % propylene, and 4.61 vol % carbon monoxide (Figure 3c and Table S5). Silk wastes yielded 40.68 vol % hydrogen gas, 35.43 vol % carbon monoxide, 2.14 vol % methane, and 0.83 vol % ethylene (Figure 3d and Table S5). The GC−MS results demonstrate that CFMP is an effective way to convert white wastes into useful fuel gases.

After each trial, residual carbon from the CFMP reaction was deposited on the carbon foam (Figure 3e−g). The residual carbon takes the form of barbs, grafted on the surface of the carbon foam (Figure 3f,g and Figure S21e). These barbs should improve the foam's ability to induce plasma discharge on the nitrogen gas by acting as a concentrator of the electric field (Figure 3e). If the graphitic carbon needles and the carbon foam are kept at the same potential, then the difference in the "radius" between the carbon foam and the needle causes a much larger external field outside the needle. This phenomenon is commonly applied in electron microscopy, where high electric fields are generated according to the following relation

$$\frac{E_{\text{tip}}}{E_0} \approx \left(\frac{a}{r}\right)^{1/2} \tag{4}$$

While the increase in efficiency has not been directly measured, these fundamental arguments based on the effects of a needle-like geometry would likely suggest that an increased efficiency of CFMP would occur over time.[38,39]

This self-perpetuating behavior is in direct contrast to traditional catalysts, which tend to deteriorate or oxidize over time,[18] reducing the reliance on expensive metals and increasing the economic incentive to adopt this system for recycling white waste. The effectiveness of CFMP should not be limited to the white wastes tested in this work. Because CFMP has shown to generate localized temperatures exceeding 3000 K, difficult-to-recycle wastes such as polytetrafluoroethylene (PTFE), keratin-based wastes such as hair, and collagen-based products like leather should also be possible. For example, TGA analysis has shown that PTFE decomposes once heated to 650 °C, with a heating rate of 25 °C min^{-1}, producing fluorocarbons, CO_2, and trace amounts of HF and hydrocarbons.[40,41] This indicates that CFMP could be a possible solution to processing PTFE waste products; however, quantifying the decomposition rate and

https://doi.org/10.1021/acs.est.0c06977
Environ. Sci. Technol. 2021, 55, 6239−6247

byproduct yields for PTFE is quite involved and would require a future study. Keratin and collagen have slightly higher decomposition temperatures compared to fibroin and sericin proteins found in silk, and a comparison of decomposition temperatures for various proteins and materials is included in Table S13.

In conclusion, a miniaturized, versatile method for recycling white wastes has been proposed and developed using a carbon foam-based microwave plasma reactor, which can be driven by intermittent renewable electricity. The CFMP process was studied and monitored with GC−MS, an *in situ* optical probe, and IR sensors. Initial experiments demonstrate the capability of CFMP to process white wastes into useful industrial regents, with hydrogen gas yield of up to 43 vol %. Additionally, the CFMP process can be used as a feeder for the Fischer−Tropsch process to convert white wastes into hydrocarbons such as ethanol, diesel, and natural gases. The formation of graphitic carbon and plasma discharge constitute a self-perpetuating chain reaction. CFMP's usage of cheap materials and its ability to process multiple plastics at once address major issues inherent in both chemical and mechanical recycling.

■ METHODS

Preparation of Carbon Foams. Carbon foams were obtained from melamine foam by a high-temperature calcination at 900 °C for 2 h with a heating rate of 3 °C min^{-1} in nitrogen.

Treatment of White Wastes. Battery separator wastes were obtained from cycled coin cells in our lab. The Celgard lithium-ion battery separator films consisted of 25 μm trilayer polypropylene-polyethylene-polypropylene membranes. Plastic and silk wastes were from abandoned bottles (polypropylene) and fabrics (silk fabric). White wastes were put on carbon foam in a sealed container (Figure 4). Then, the sealed container with nitrogen was put into microwave oven (Figure 2a). These white wastes were treated on the carbon foam with a microwave plasma reactor at different length scales and power outputs. The microwave oven was operated at a microwave frequency of 2.45 GHz and a maximum output of 1100 W (Panasonic, NN-SU696S).

Materials Characterization. Scanning electron microscopy (SEM) and scanning transmission electron microscopy (STEM) were performed on a Zeiss Merlin high-resolution SEM. Thermogravimetric analysis (TGA) was performed on a NETZSCH STA 409 PC TGA-DSC instrument under a N_2 atmosphere at a heating rate of 10 °C min^{-1} from 30 to 900 °C. Transmission electron microscopy (TEM) was carried out on a JEOL 2010F model. Compression experiments were carried out on a dynamic mechanical analysis (DMA) Q850 model (TA Instruments, New Castle, DE) with a loading speed of 0.5 mm min^{-1} at room temperature, and 3 samples were tested in total for repeatability. X-ray photoelectron spectroscopy (XPS) analysis was performed on a PerkinElmer PHI 550 spectrometer with Al Kα radiation (1486.6 eV) as the X-ray source. Gamma irradiation measurements were conducted on a Gammacell Irradiator (220 Excel self-shielded high dose rate gamma ray). The N_2 adsorption/desorption tests were performed by Brunauer−Emmett−Teller (BET) measurements on an ASAP-2010 surface area analyzer. Pore size distribution (PSD) was derived from the adsorption branch of the isotherm by the Barrett−Joyner−Halenda (BJH) method. The X-ray diffraction (XRD) patterns were recorded on a Bruker-AXS D8 DISCOVER. Room temperature Raman spectroscopy was conducted with a Jobin Yvon HR800 confocal Raman system with a 632.8 nm diode-laser excitation on a 300 S mm^{-1} line grating. *In situ* light spectrum data was recorded on an FX2000-EX type fiber optic spectrometer. Gas composition was analyzed with a refinery gas analyzer (HP Agilent 7890 A) by the ASTM D1945-14 method. H_2, CO, CO_2, N_2, and O_2 were analyzed on the thermal conductivity detector (TCD) channels. Hydrocarbons were analyzed on the flame-ionization detector (FID) channel. The response factor was obtained using a refinery gas analysis calibration gas standard for quantitative analysis.

Simulation. All parts made in SolidWorks 2020 were treated as solid bodies and included the following materials from the software's database: glass (for the beaker), copolymer (for the plastic/mask sample), and plain carbon steel (for the microwave enclosure). Two custom materials were implemented: ceramic insulation based on FiberFax and carbon foam. Further improvement of the thermal analysis, from a materials selection perspective, could be made with more exact thermal properties for the carbon foam. However, besides convection from the outside of the microwave to the ambient region, radiation is assumed to be the main mechanism for heat transfer. Therefore, according to eq 3, temperature and exposed areas are the driving factors for this analysis. Further information such as the part shapes, material properties, mesh information, and thermal loads are summarized in Table S6−S12.

■ ASSOCIATED CONTENT

Supporting Information

The Supporting Information is available free of charge at https://pubs.acs.org/doi/10.1021/acs.est.0c06977.

(Video S1) Carbon foam demonstrating sufficient mechanical properties (MP4)

(Video S2) Local high temperature recorded by an in situ infrared sensor (MP4)

(Video S3) Ceramic fiber blankets used to insulate the CFMP system (MP4)

(Video S4) Initial experiment at 110 W with a reaction time of 8 s (MP4)

(Video S5) Initial experiment at 220 W with a reaction time of 8 s (MP4)

(Video S6) Initial experiment at 330 W with a reaction time of 8 s (MP4)

(Video S7) Experiment at 330 W with a reaction time of 4 s (MP4)

(Video S8) Experiment at 330 W with a reaction time of 12 s (MP4)

(Figures S1−S23 and Tables S1−S15) Additional information, characterization, analysis results, and images of the battery waste separator (PDF)

■ AUTHOR INFORMATION

Corresponding Authors

Jinliang Qiao − *SINOPEC Beijing Research Institute of Chemical Industry, Beijing 100013, China;* orcid.org/0000-0002-2608-6223; Email: qiaojl.bjhy@sinopec.com

Meifang Zhu − *State Key Laboratory for Modification of Chemical Fibers and Polymer Materials, College of Materials Science and Engineering, Donghua University, Shanghai 201620, China;* orcid.org/0000-0003-0359-3633; Email: zmf@dhu.edu.cn

Ju Li − *Department of Nuclear Science and Engineering and Department of Materials Science and Engineering, Massachusetts Institute of Technology, Cambridge,*

https://doi.org/10.1021/acs.est.0c06977
Environ. Sci. Technol. 2021, 55, 6239−6247

Massachusetts 02139, United States; orcid.org/0000-0002-7841-8058; Email: liju@mit.edu

Authors

Guiyin Xu − *Department of Nuclear Science and Engineering, Massachusetts Institute of Technology, Cambridge, Massachusetts 02139, United States;* orcid.org/0000-0002-5959-4814

Haibin Jiang − *Department of Nuclear Science and Engineering, Massachusetts Institute of Technology, Cambridge, Massachusetts 02139, United States; SINOPEC Beijing Research Institute of Chemical Industry, Beijing 100013, China*

Myles Stapelberg − *Department of Nuclear Science and Engineering, Massachusetts Institute of Technology, Cambridge, Massachusetts 02139, United States*

Jiawei Zhou − *Department of Mechanical Engineering, Massachusetts Institute of Technology, Cambridge, Massachusetts 02139, United States*

Mengyang Liu − *College of Ocean & Earth Sciences, Xiamen University, Xiamen 361102, China*

Qing-Jie Li − *Department of Nuclear Science and Engineering, Massachusetts Institute of Technology, Cambridge, Massachusetts 02139, United States*

Yunteng Cao − *Department of Civil and Environmental Engineering, Massachusetts Institute of Technology, Cambridge, Massachusetts 02139, United States;* orcid.org/0000-0002-6425-7628

Rui Gao − *Department of Nuclear Science and Engineering, Massachusetts Institute of Technology, Cambridge, Massachusetts 02139, United States*

Minggang Cai − *College of Ocean & Earth Sciences, Xiamen University, Xiamen 361102, China*

Mitchell S Galanek − *Environment, Health & Safety Office, Massachusetts Institute of Technology, Cambridge, Massachusetts 02139, United States*

Weiwei Fan − *Department of Nuclear Science and Engineering, Massachusetts Institute of Technology, Cambridge, Massachusetts 02139, United States*

Weijiang Xue − *Department of Nuclear Science and Engineering, Massachusetts Institute of Technology, Cambridge, Massachusetts 02139, United States;* orcid.org/0000-0002-3060-4580

Benedetto Marelli − *Department of Civil and Environmental Engineering, Massachusetts Institute of Technology, Cambridge, Massachusetts 02139, United States;* orcid.org/0000-0001-5311-6961

Complete contact information is available at: https://pubs.acs.org/10.1021/acs.est.0c06977

Notes

The authors declare no competing financial interest.

■ ACKNOWLEDGMENTS

We acknowledge support by Yintai Investment Co., LLC. B.M. acknowledges support from the Office of Naval Research (ONR award N00014-18-12258) and the National Science Foundation (NSF award CMMI-1752172).

■ REFERENCES

(1) Hoornweg, D.; Bhada-Tata, P.; Kennedy, C. Environment: Waste production must peak this century. *Nature* **2013**, *502*, 615−617.

(2) You, S.; Sonne, C.; Ok, Y. S. COVID-19's unsustainable waste management. *Science* **2020**, *368*, 1438.1.

(3) *The plastic pandemic is only getting worse during COVID-19*; World Economic Forum: 2020 https://www.weforum.org/agenda/2020/07/plastic-waste-management-covid19-ppe/.

(4) Jambeck, J. R.; Geyer, R.; Wilcox, C.; Siegler, T. R.; Perryman, M.; Andrady, A.; Narayan, R.; Law, K. L. Plastic waste inputs from land into the ocean. *Science* **2015**, *347*, 768−771.

(5) *Plastic Can Take 500 Years To Bio-Degrade In The Ocean*; Manufacturing.net: 2018 https://www.statista.com/chart/15905/the-estimated-number-of-years-for-selected-items-to-bio-degrade/.

(6) de Souza Machado, A. A.; Kloas, W.; Zarfl, C.; Hempel, S.; Rillig, M. C. Microplastics as an emerging threat to terrestrial ecosystems. *Glob. Chang. Biol.* **2018**, *24*, 1405−1416.

(7) Auta, H. S.; Emenike, C. U.; Fauziah, S. H. Distribution and importance of microplastics in the marine environment: A review of the sources, fate, effects, and potential solutions. *Environ. Int.* **2017**, *102*, 165−176.

(8) Lusher, A. L.; Tirelli, V.; O'Connor, I.; Officer, R. Microplastics in Arctic polar waters: the first reported values of particles in surface and sub-surface samples. *Sci. Rep.* **2015**, *5*, 14947.

(9) Eriksen, M.; Mason, S.; Wilson, S.; Box, C.; Zellers, A.; Edwards, W.; Farley, H.; Amato, S. Microplastic pollution in the surface waters of the Laurentian Great Lakes. *Mar. Pollut. Bull.* **2013**, *77*, 177−182.

(10) Isobe, A.; Uchiyama-Matsumoto, K.; Uchida, K.; Tokai, T. Microplastics in the Southern Ocean. *Mar. Pollut. Bull.* **2017**, *114*, 623−626.

(11) Mu, J.; Zhang, S.; Qu, L.; Jin, F.; Fang, C.; Ma, X.; Zhang, W.; Wang, J. Microplastics abundance and characteristics in surface waters from the Northwest Pacific, the Bering Sea, and the Chukchi Sea. *Mar. Pollut. Bull.* **2019**, *143*, 58−65.

(12) Garcia, J. M.; Robertson, M. L. The future of plastics recycling. *Science* **2017**, *358*, 870−872.

(13) Rahimi, A.; García, J. M. Chemical recycling of waste plastics for new materials production. *Nat. Rev. Chem.* **2017**, *1*, 0046.

(14) Ressourceneffizienz, V. Z. Recycling plastics−Resource efficiency with an optimized sorting method. Recovery recycling technology Wolrdwide: https://www.youtube.com/watch?v=I_fUpP-hq3A 2018.

(15) Guha Roy, A. Detailing plastic pollution. *Nat. Sustain.* **2019**, *2*, 654−654.

(16) Zhang, Z.; Gora-Marek, K.; Watson, J. S.; Tian, J.; Ryder, M. R.; Tarach, K. A.; López-Pérez, L.; Martínez-Triguero, J.; Melián-Cabrera, I. Recovering waste plastics using shape-selective nano-scale reactors as catalysts. *Nat. Sustain.* **2019**, *2*, 39−42.

(17) https://en.wikipedia.org/wiki/Microwave_oven#cite_note-1.

(18) Sun, J.; Wang, W.; Yue, Q.; Ma, C.; Zhang, J.; Zhao, X.; Song, Z. Review on microwave−metal discharges and their applications in energy and industrial processes. *Appl. Energy* **2016**, *175*, 141−157.

(19) Menéndez, J. A.; Arenillas, A.; Fidalgo, B.; Fernández, Y.; Zubizarreta, L.; Calvo, E. G.; Bermúdez, J. M. Microwave heating processes involving carbon materials. *Fuel Process. Technol.* **2010**, *91*, 1−8.

(20) Tiwari, S.; Caiola, A.; Bai, X.; Lalsare, A.; Hu, J. Microwave plasma-enhanced and microwave heated chemical reactions. *Plasma Chem. Plasma Process.* **2020**, *40*, 1−23.

(21) Hawtof, R.; Ghosh, S.; Guarr, E.; Xu, C.; Mohan Sankaran, R.; Renner, J. N. Catalyst-free, highly selective synthesis of ammonia from nitrogen and water by a plasma electrolytic system. *Sci. Adv.* **2019**, *5*, eaat5778.

(22) Sun, J.; Wang, Q.; Wang, W.; Song, Z.; Zhao, X.; Mao, Y.; Ma, C. Novel treatment of a biomass tar model compound via microwave-metal discharges. *Fuel* **2017**, *207*, 121−125.

(23) Khattak, H. K.; Bianucci, P.; Slepkov, A. D. Linking plasma formation in grapes to microwave resonances of aqueous dimers. *Proc. Natl. Acad. Sci. U. S. A.* **2019**, *116*, 4000−4005.

(24) Xu, S.; Zhong, G.; Chen, C.; Zhou, M.; Kline, D. J.; Jacob, R. J.; Xie, H.; He, S.; Huang, Z.; Dai, J.; Brozena, A. H.; Shahbazian-Yassar, R.; Zachariah, M. R.; Anlage, S. M.; Hu, L. Uniform, scalable, high-

temperature microwave shock for nanoparticle synthesis through defect engineering. *Matter* **2019**, *1*, 759−769.
(25) Wang, W.; Fu, L.; Sun, J.; Grimes, S.; Mao, Y.; Zhao, X.; Song, Z. Experimental study of microwave-induced discharge and mechanism analysis based on spectrum acquisition. *IEEE Trans. Plasma Sci.* **2017**, *45*, 2235−2242.
(26) Huang, H.; Zhou, S.; Yu, C.; Huang, H.; Zhao, J.; Dai, L.; Qiu, J. Rapid and energy-efficient microwave pyrolysis for high-yield production of highly-active bifunctional electrocatalysts for water splitting. *Energy Environ. Sci.* **2020**, *13*, 545−553.
(27) Xu, G.; Han, J.; Ding, B.; Nie, P.; Pan, J.; Dou, H.; Li, H.; Zhang, X. Biomass-derived porous carbon materials with sulfur and nitrogen dual-doping for energy storage. *Green Chem.* **2015**, *17*, 1668−1674.
(28) Xu, G.; Yu, D.; Zheng, D.; Wang, S.; Xue, W.; Cao, X. E.; Zeng, H.; Xiao, X.; Ge, M.; Lee, W. K.; Zhu, M. Fast heat transport inside lithium-sulfur batteries promotes their safety and electrochemical performance. *iScience* **2020**, *23*, 101576.
(29) Chen, L.; Alshawabkeh, A. N.; Hojabri, S.; Sun, M.; Xu, G.; Li, J. A robust flow-through platform for organic contaminant removal. *Cell Rep. Phys. Sci.* **2021**, *2*, 100296.
(30) *NIST Atomic Spectra Database Lines Form*; National Institute of Standards and Technology: https://physics.nist.gov/PhysRefData/ASD/lines_form.html.
(31) Black-body radiation https://en.wikipedia.org/wiki/Black-body_radiation.
(32) https://www.youtube.com/watch?v=zJsUrhRVVVw&feature=emb_err_woyt.
(33) https://www.youtube.com/watch?v=r5g5Kjed3og&feature=emb_logo.
(34) https://www.youtube.com/watch?v=OMF8np_gs7Q.
(35) Lancet, M. S.; Anders, E. Carbon isotope fractionation in the Fischer-Tropsch synthesis and in meteorites. *Science* **1970**, *170*, 980−982.
(36) Xu, G.; Kushima, A.; Yuan, J.; Dou, H.; Xue, W.; Zhang, X.; Yan, X.; Li, J. *Ad hoc* solid electrolyte on acidized carbon nanotube paper improves cycle life of lithium−sulfur batteries. *Energy Environ. Sci.* **2017**, *10*, 2544−2551.
(37) Xu, G.; Nie, P.; Dou, H.; Ding, B.; Li, L.; Zhang, X. Exploring metal organic frameworks for energy storage in batteries and supercapacitors. *Mater. Today* **2017**, *20*, 191−209.
(38) Fricker, H. S. Why does charge concentrate on points? *Phys. Educ.* **1989**, *24*, 157−161.
(39) Duxbury, P.M. *PHY294H - Electricity and magnetism (Honors)*; Academic Press: https://web.pa.msu.edu/people/duxbury/courses/phy294H/phy294H.html.
(40) Conesa, J. A.; Font, R. Polytetrafluoroethylene decomposition in air and nitrogen. *Polym. Eng. Sci.* **2001**, *41*, 2137−2147.
(41) Wall, L. A.; Michaelsen, J. D. Thermal decomposition of polytetrafluoroethylene in various gaseous atmospheres. *J. Res. Natl. Bur. Stand.* **1956**, *56*, 27.

https://doi.org/10.1021/acs.est.0c06977
Environ. Sci. Technol. 2021, 55, 6239−6247

Supporting Information

Self-perpetuating Carbon-foam Microwave Plasma Conversion of Hydrocarbon Wastes into Useful Fuels and Chemicals

Guiyin Xu[1], Haibin Jiang[1,2], Myles Stapelberg[1], Jiawei Zhou[3], Mengyang Liu[4], Qing-Jie Li[1], Yunteng Cao[5], Rui Gao[1], Minggang Cai[4], Jinliang Qiao*[2], Mitchell S Galanek[6], Weiwei Fan[1], Weijiang Xue[1], Benedetto Marelli[5], Meifang Zhu*[7], Ju Li*[1,8]

[1]Department of Nuclear Science and Engineering, Massachusetts Institute of Technology, Cambridge, MA 02139, USA

[2]SINOPEC Beijing Research Institute of Chemical Industry, Beijing 100013, China

[3]Department of Mechanical Engineering, Massachusetts Institute of Technology, Cambridge, MA 02139, USA

[4]College of Ocean & Earth Sciences, Xiamen University, Xiamen 361102, China

[5]Department of Civil and Environmental Engineering, Massachusetts Institute of Technology, Cambridge, MA 02139, USA

[6]Environment, Health & Safety Office, Massachusetts Institute of Technology, Cambridge, MA 02139, USA

[7]State Key Laboratory for Modification of Chemical Fibers and Polymer Materials, College of Materials Science and Engineering, Donghua University, Shanghai 201620, China

[8]Department of Materials Science and Engineering, Massachusetts Institute of Technology, Cambridge, MA 02139, USA

*Correspondence to: Jinliang Qiao (qiaojl.bjhy@sinopec.com); Meifang Zhu (zmf@dhu.edu.cn); Ju Li (liju@mit.edu)

(44 Pages, 23 Figures, and 15 Tables)

Figure S1. The digital images of (a) silk waste and (b) batteries separator waste. The treatment process of wastes: (c) incineration and (d) utilization.

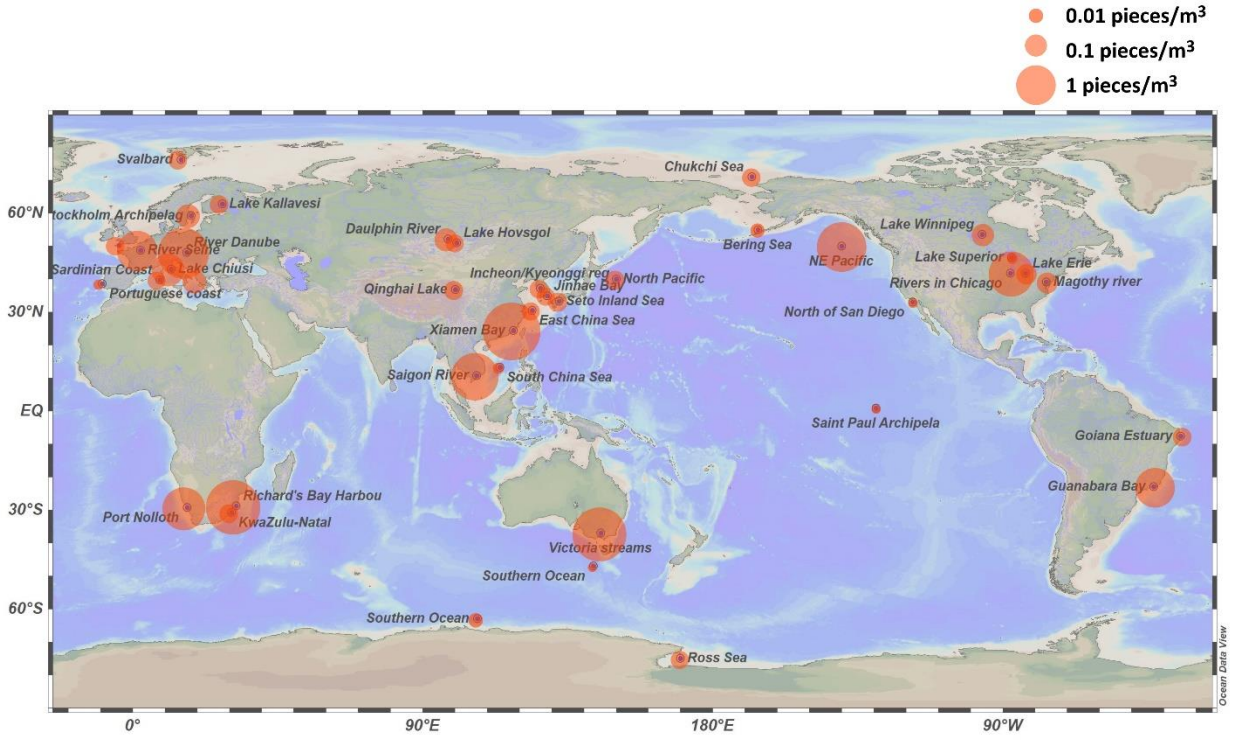

Figure S2. Abundances of microplastics from marine environments, including lakes, rivers, seas, and oceans.

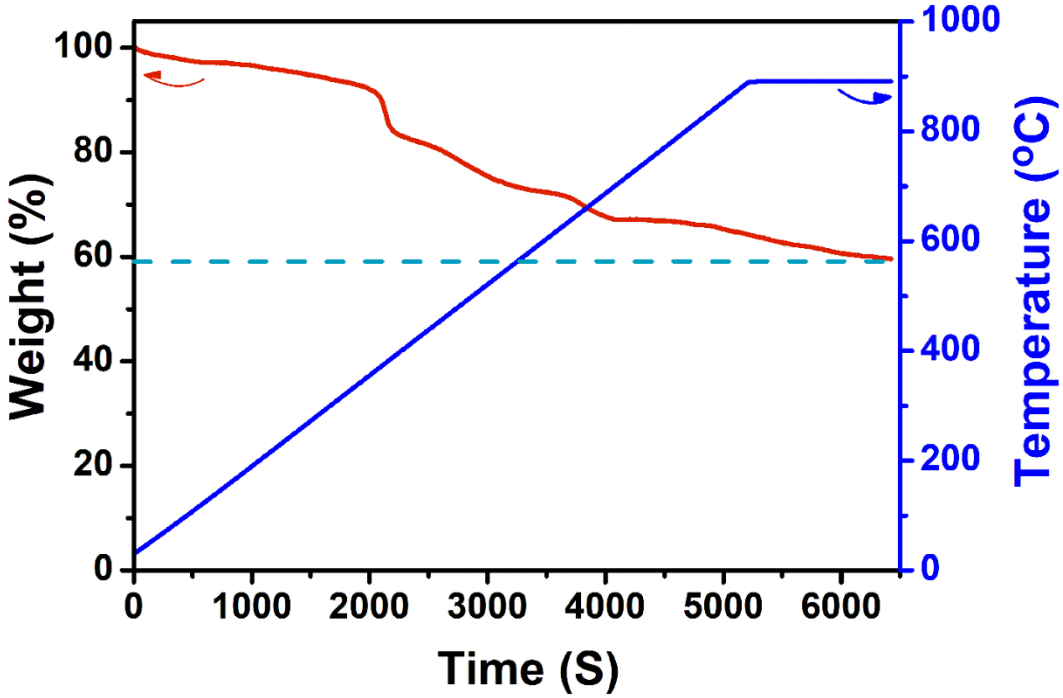

Figure S3. Thermal gravimetric (TG) curves of the carbon foam made by the pyrolysis of melamine foam under an inert atmosphere.

Thermal gravimetric (TG) analysis was conducted on a TG-DSC instrument (NETZSCH STA 409 PC) under a N_2 atmosphere at a heating rate of 10 °C min^{-1} from 30 to 900 °C. After the constant temperature treatment at 900 °C, the weight curve stabilizes, with a yield up to 60%.

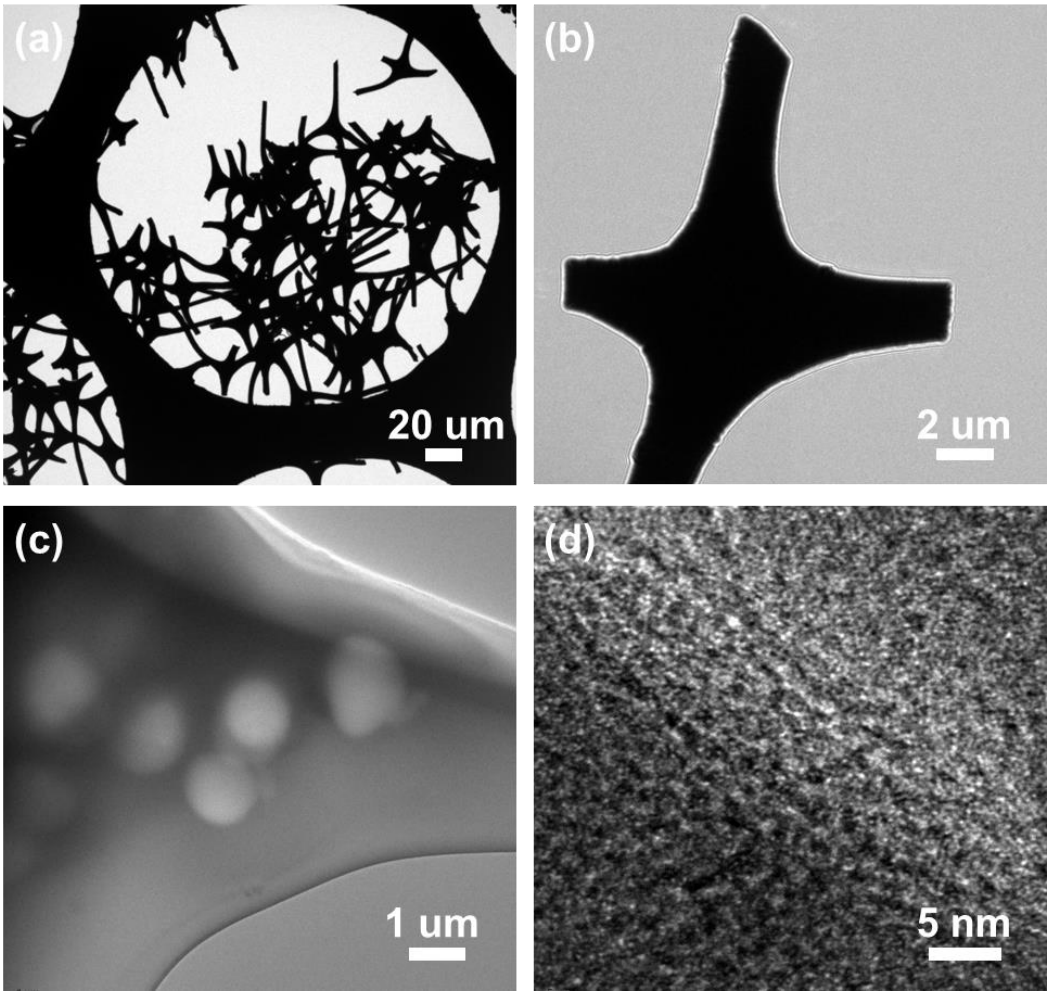

Figure S4. (a-c) Transmission electron microscopy (TEM) and (d) high-resolution transmission electron microscopy (HRTEM) images of the carbon foam.

TEM images presented the structure of the carbon foam (**Figure S4a, b**). Macropores on the surface of carbon foam (**Figure S4c**) are from the decomposition of melamine and additional micropores and mesopores are observed under high resolution transmission electron microscopy (HRTEM) (**Figure S4d**).

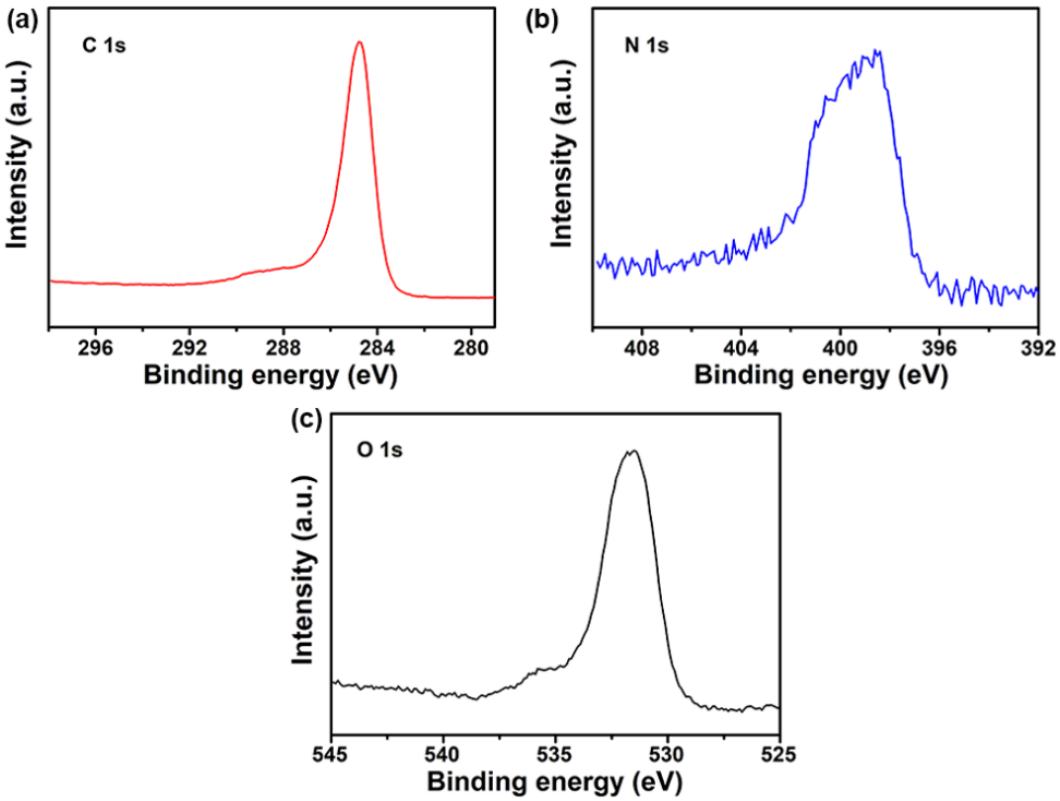

Figure S5. (a) C 1s, (b) N 1s, and (c) O 1s X-ray photoelectron spectroscopy (XPS) spectra for the carbon foam.

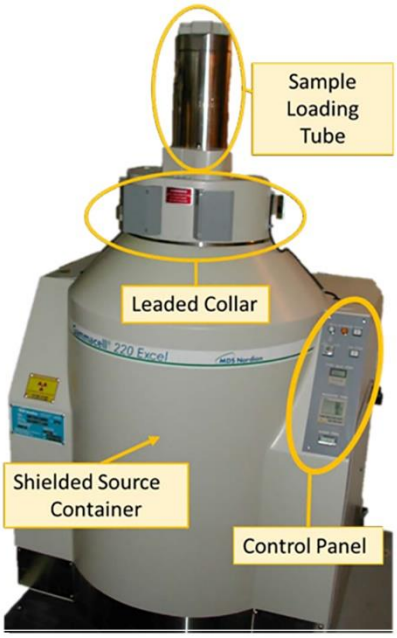

Figure S6. The image of Gammacell Irradiator (220 Excel self-shielded high dose rate gamma ray) in MIT. Gamma and microwaves are both forms of electromagnetic waves, albeit gamma rays have much shorter frequencies and higher energies associated with them. Therefore, gamma rays can serve as a stress test on the carbon foam to estimate its resistance to radiation.

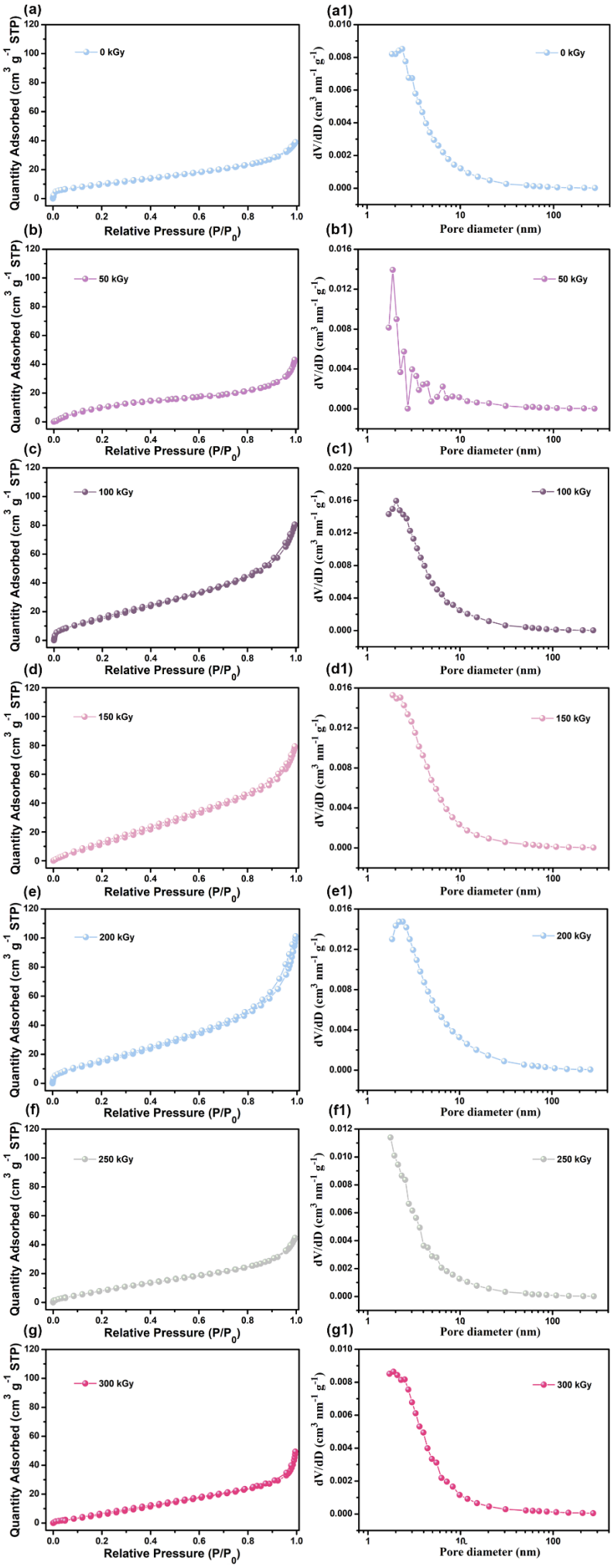
(a)
0 kGy
Quantity Adsorbed (cm3 g-1 STP)
Relative Pressure (P/P0)
(a1)
0 kGy
dV/dD (cm3 nm-1 g-1)
Pore diameter (nm)
(b)
50 kGy
(b1)
50 kGy
(c)
100 kGy
(c1)
100 kGy
(d)
150 kGy
(d1)
150 kGy
(e)
200 kGy
(e1)
200 kGy
(f)
250 kGy
(f1)
250 kGy
(g)
300 kGy
(g1)
300 kGy

Figure S7. N_2 adsorption/desorption isotherms at 77 K and Pore size distribution (PSD) curves of the carbon foam irradiated at different kGy doses: (a, a1) 0, (b, b1) 50, (c, c1) 100, (d, d1) 150, (e, e1) 200, (f, f1) 250, (g, g1) 300 does. PSD was calculated using the Barrett-Joyner-Halenda (BJH) method.

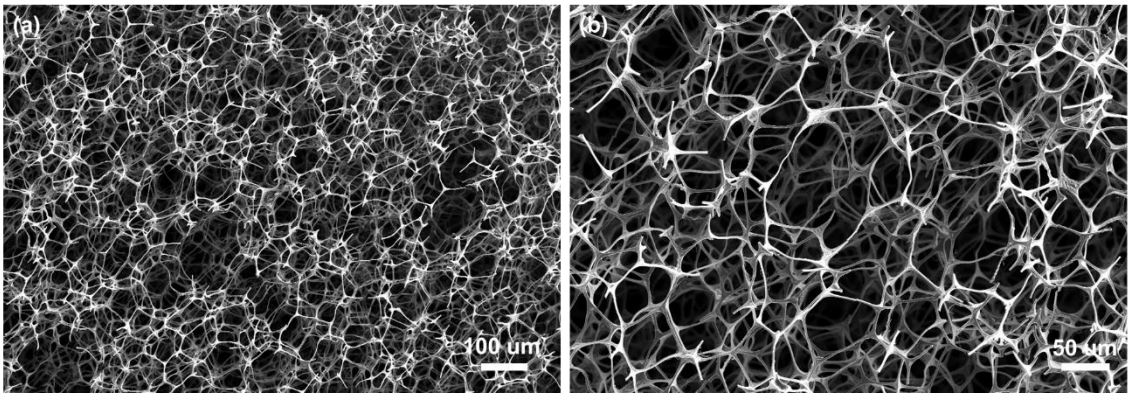

Figure S8. Scanning electron microscopy (SEM) image of the carbon foam irradiated at 50 kGy doses.

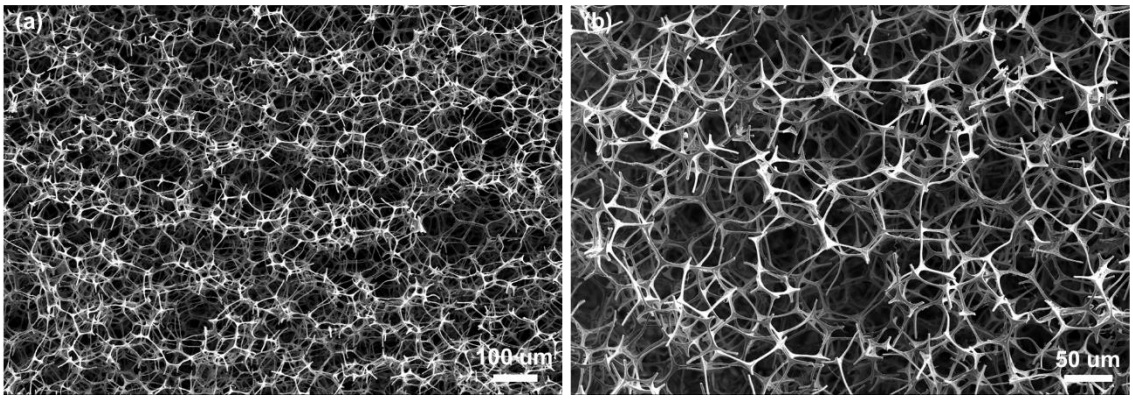

Figure S9. Scanning electron microscopy (SEM) image of the carbon foam irradiated at 100 kGy doses.

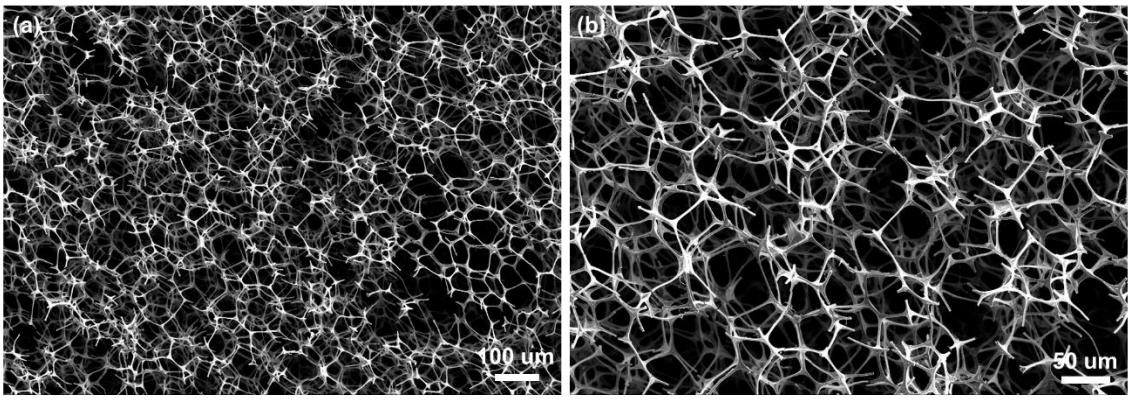

Figure S10. Scanning electron microscopy (SEM) image of the carbon foam irradiated at 150 kGy doses.

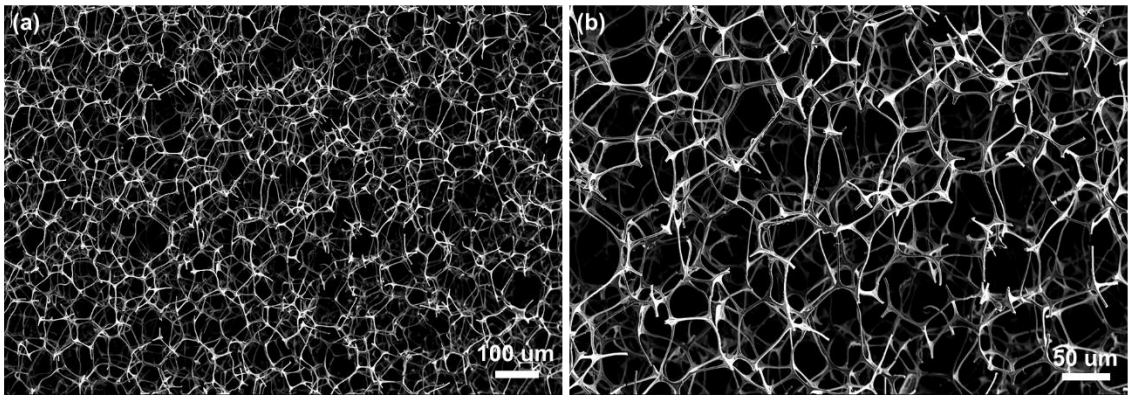

Figure S11. Scanning electron microscopy (SEM) image of the carbon foam irradiated at 200 kGy doses.

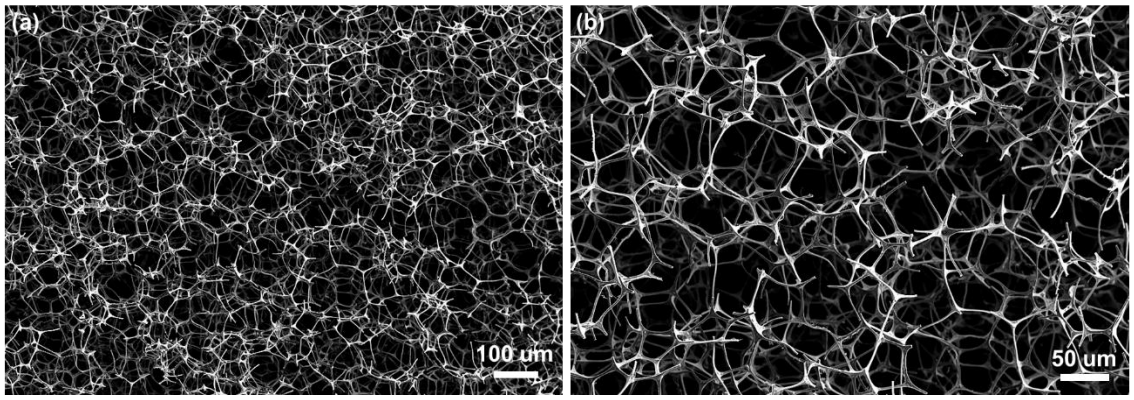

Figure S12. Scanning electron microscopy (SEM) image of the carbon foam irradiated at 250 kGy doses.

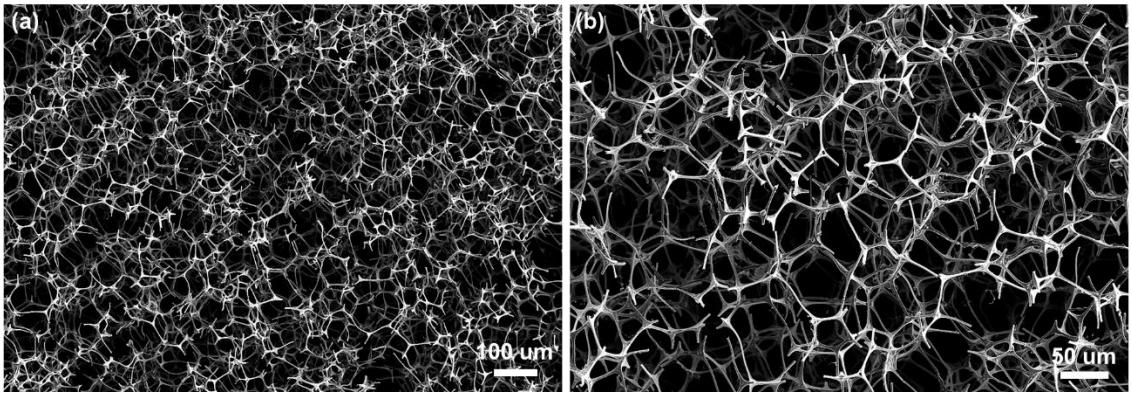

Figure S13. Scanning electron microscopy (SEM) image of the carbon foam irradiated at 300 kGy doses.

Figure S14. Thermal images of the microwave plasma reactor. Prior to running the process, thermal images were measured with an infrared camera.

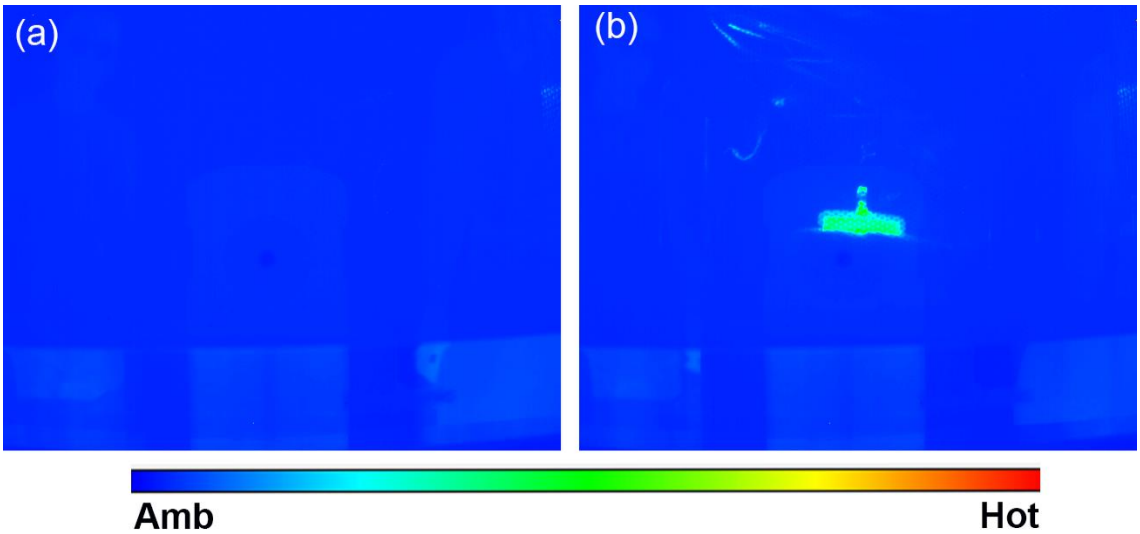

Figure S15. Thermal images of the microwave plasma reactor at (a) 0 s, and (b) a few seconds after irradiation. Transient temperature changes are shown in **Video S3**. To clearly show that the sample heats up quickly once the plasma is ignited, we removed some ceramic fiber blankets and exposed the center part of the carbon foam (**Video S2**). The linear color scale represents the ambient and hot temperature.

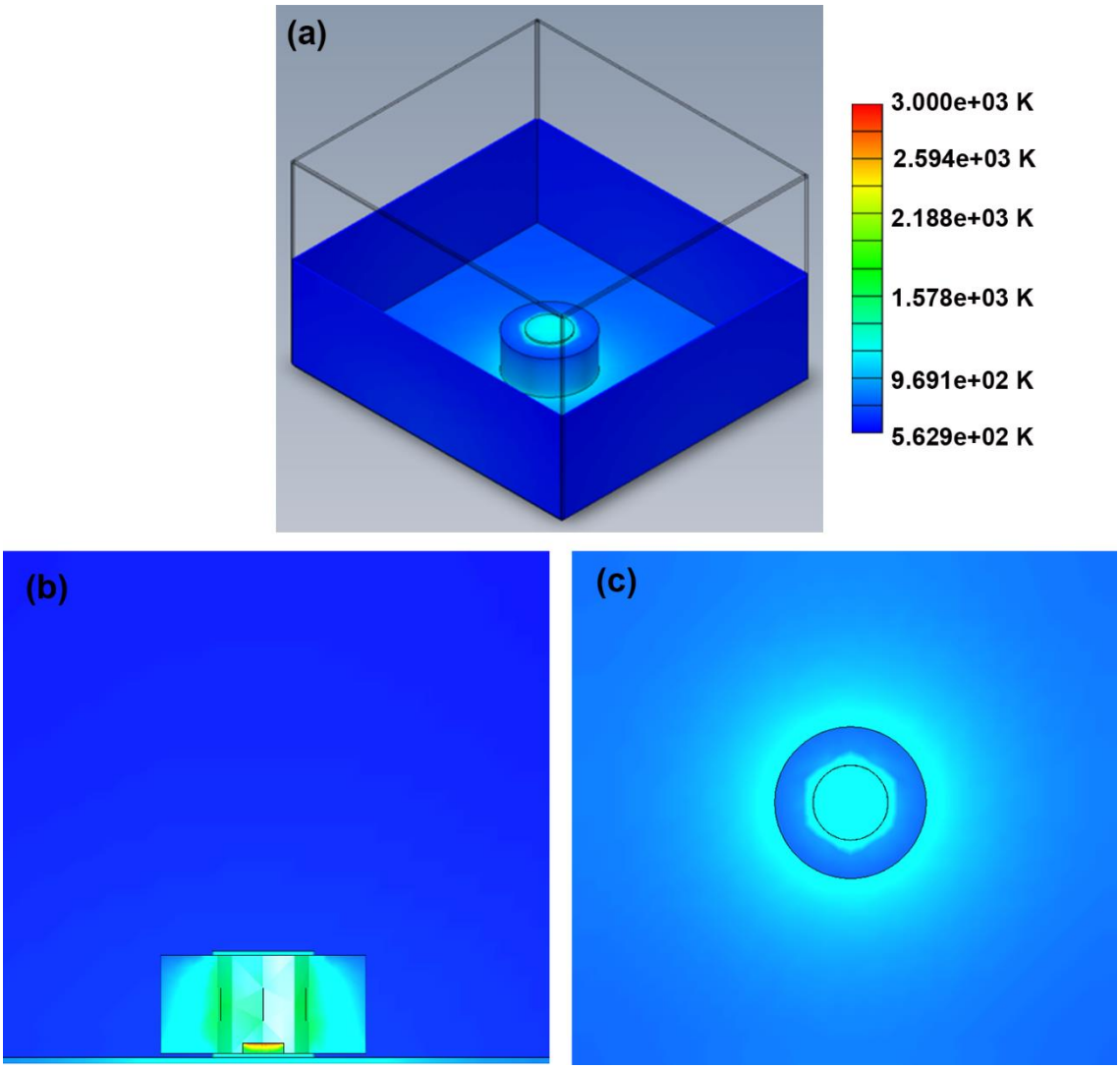

Figure S16. (a) 45 degree profile, (b) side profile, (c) top down view of steady state thermal analysis done in SolidWorks.

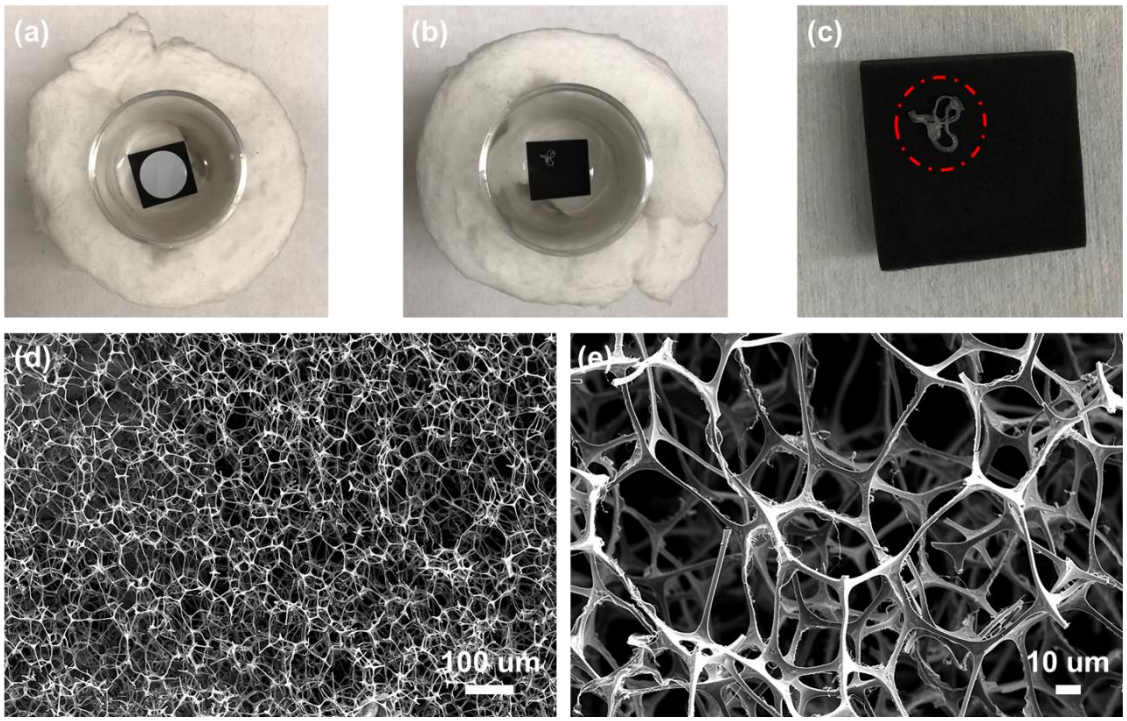

Figure S17. Images of battery separator waste on the carbon foam (a) before and (b, c) after the microwave irradiation with 110 W for 8 s. (d, e) Scanning electron microscopy (SEM) images of the carbon foam with battery separator waste after 110 W and 8 s. The dynamic process was recorded in **Video S4**.

As shown in the SEM result (**Figure S17e**), carbon particles are deposited on the surface of the carbon foam.

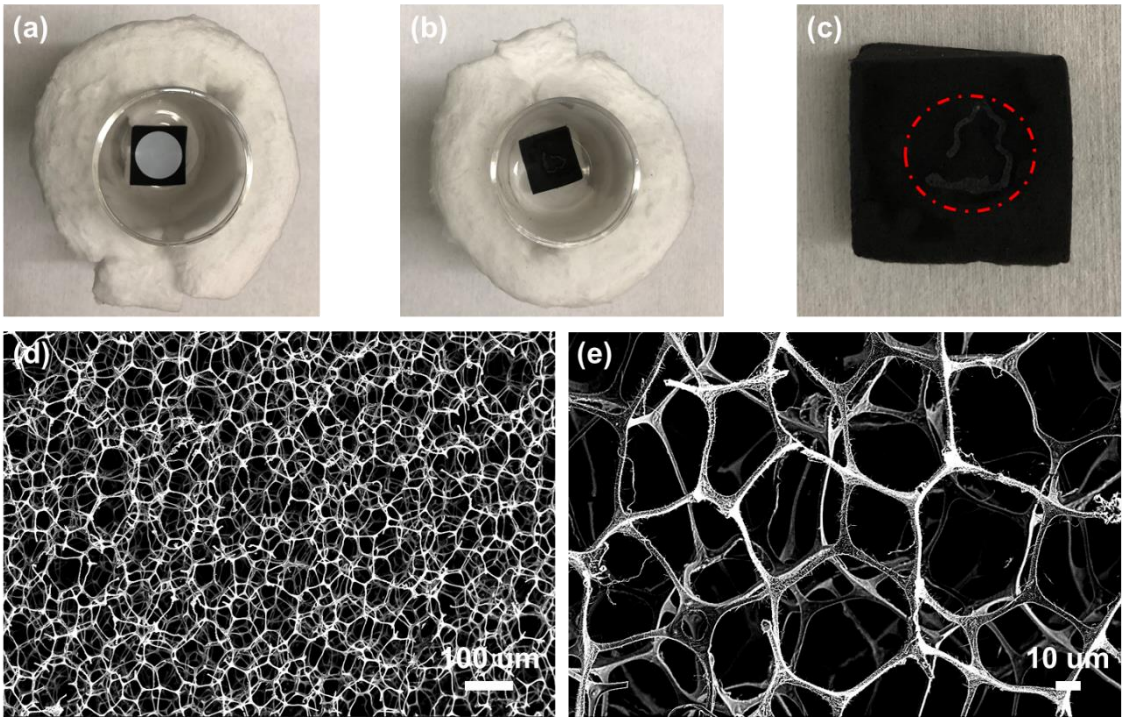

Figure S18. Images of battery separator waste on the carbon foam (a) before and (b, c) after the microwave irradiation with 220 W for 8 s. (d, e) Scanning electron microscopy (SEM) images of the carbon foam with battery separator waste after 220 W and 8 s. The dynamic process was recorded in **Video S5**.

As shown in the SEM result (**Figure S18e**), carbon particles and few thorn-like carbons are deposited on the carbon foam.

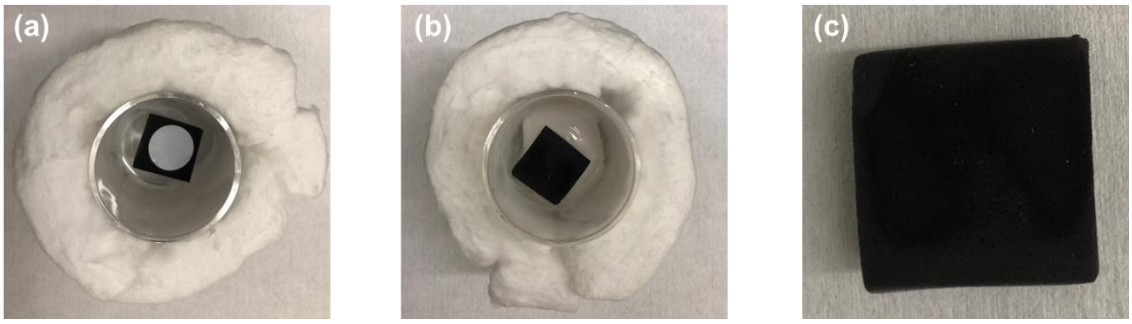

Figure S19. Images of battery separator waste on the carbon foam (a) before and (b, c) after the microwave irradiation at 330 W for 8 s. The dynamic process was recorded in **Video S6**.

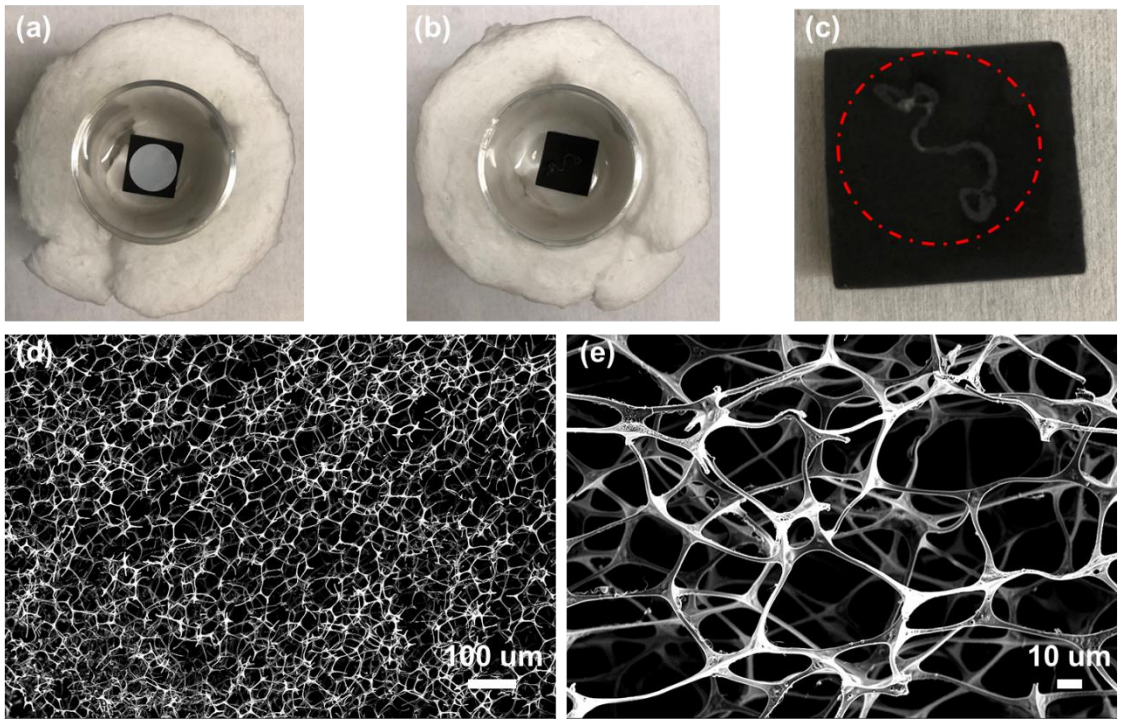

Figure S20. Images of battery separator waste on the carbon foam (a) before and (b, c) after the microwave irradiation at 330 W for 4 s. (d, e) Scanning electron microscopy (SEM) images of the carbon foam with batteries separator waste after 330 W and 4 s. The dynamic process was recorded in **Video S7**.

As shown in the SEM result (**Figure S20e**), carbon particles are deposited on the surface of the carbon foam.

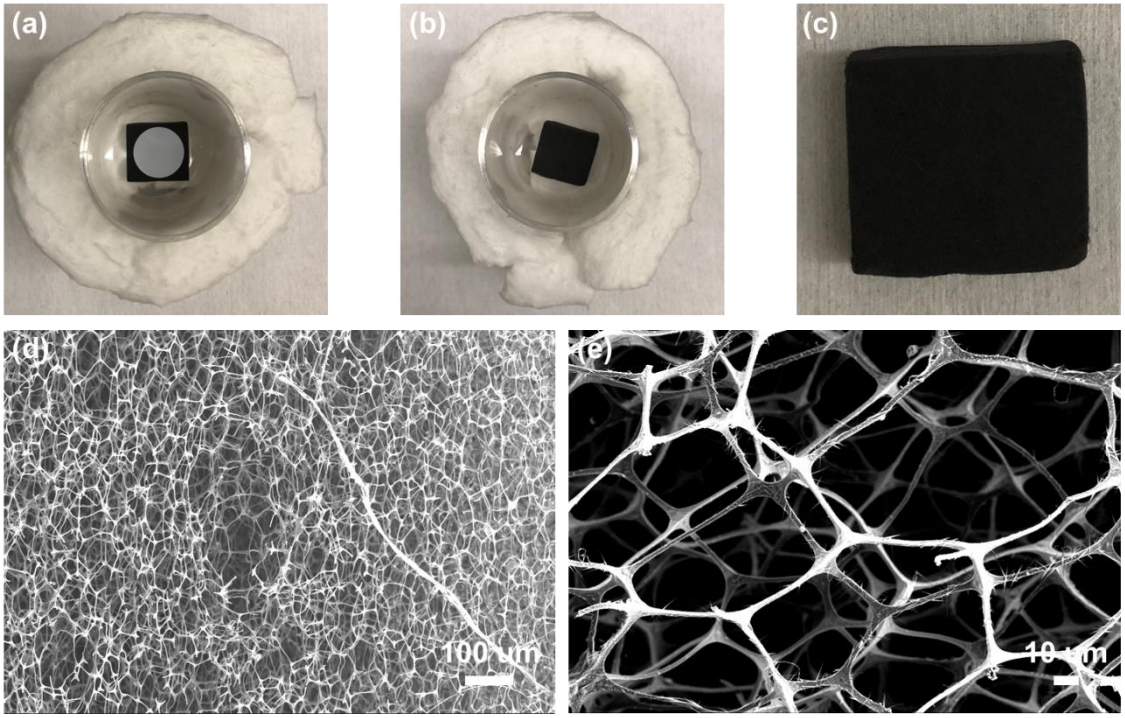

Figure S21. Images of battery separator waste on the carbon foam (a) before and (b, c) after the microwave irradiation at 330 W for 12 s. (d, e) Scanning electron microscopy (SEM) images of the carbon foam with batteries separator waste after 330 W and 12 s. The dynamic process was recorded in **Video S8**.

Many carbon atoms were grafted on the surface of the carbon foam (**Figure S21e**) forming barbs similar to the experimental conditions of 330W, 8s (**Figure 3g**).

Table S1. Abundances (pieces/m^3) of microplastics in surface waters worldwide, including lakes, rivers, seas and oceans.

Location	Mean Abundance	Reference
Lake Superior	0.037	1
Lake Erie	0.66	
Lake Hovsgol	0.12	2
River Seine	30	3
River Danube	320	4
Rivers in Chicago	6	5
Magothy river	0.75	6
Lake Chiusi	3.36	7
Daulphin River	1.23	8
Qinghai Lake	0.36	9
Lake Kallavesi	0.27	10
Goiana Estuary	0.26	11
Victoria streams	400	12
KwaZulu-Natal	0.27	13
Saigon River	223	14
Guanabara Bay	11.5	15
Stockholm Archipelago, Baltic Sea	1.37	16
Xiamen Bay	500	17
Richard's Bay Harbor	413	18
Port Nolloth	100	18
NE Pacific	279	19
Strait of Georgia	3210	20
Seto Inland Sea	0.39	21
Svalbard	0.34	22
Saint Paul Archipelago	0.01	23
North of San Diego	0.016	24
Western English Channel	0.27	25
Incheon/Kyeonggi region	0.19	26
Jinhae Bay	0.182	27
Sardinian Coast	0.15	28
Chukchi Sea	0.23	29
Bering Sea	0.097	29
Southern Ocean	0.1	30
Portuguese coast	0.028	31
East China Sea	0.167	32

Note: All the results have been in pieces/m^3.

Table S2. Literature review of other waste and greenhouse gas recycling methods utilizing microwaves, with or without catalyst-assisted plasma discharge.

Process	Catalyst	Duration	Byproduct	Ref
Microwave Dehydrogenation for Plastic Wastes	$FeAlO_x$	30-90 s	H_2 + MWCNT	33
Cold-Plasma Vegetable Oil Cracking	Tungsten	40 minutes	Hexadecane	34
Microwave-Assisted Dry Reforming (MADR) for CH_4 and CO_2	Char	~2 hours	Syngas	35
MADR for CH_4 and CO_2	Activated Carbon	300 minutes	H_2 + CO	36
Microwave Discharge	Carbon Coated Aluminum Oxide Fibers	40 s	Ethylene, Propylene, H_2, CO, CH_4, C, hydrocarbons	37
Microwave Pyrolysis of Baby Diapers	Activated Carbon	15 minutes	$C_2H_4O_2$, C_3H_4O, CO, H_2O, $C_3H_6O_3$, esters, alkanes, and alkenes	38

Table S3. BET surface area, pore volume, and pore size of the carbon foam irradiated at different kGy doses (0, 50, 100, 150, 200, 250, 300 does).

Samples	BET Surface Area (m^2 g^{-1})	Pore Volume (cm^3 g^{-1})	Pore Size (nm)
Carbon Foam (0 kGy)	36.3160	0.055634	6.1463
Carbon Foam (50 kGy)	53.8853	0.053073	7.2974
Carbon Foam (100 kGy)	60.5879	0.117556	6.4004
Carbon Foam (150 kGy)	65.9787	0.111444	6.4686
Carbon Foam (200 kGy)	59.7078	0.146889	7.8720
Carbon Foam (250 kGy)	36.7745	0.062815	6.2607
Carbon Foam (300 kGy)	29.6457	0.070289	6.9696

Table S4. The peaks in Figure 3b correspond to the transitions between the different electronic levels in carbon and nitrogen.

Species	Observed Wavelength Vac (nm)	Ritz Wavelength Vac (nm)	Transition
C II	357.92	358.1757	$2s2p(^3P^\circ)3p \rightarrow 2s2p(^3P^\circ)4s$
N II	387.00	386.4318	$2s^22p4p \rightarrow 2s2p^2(^4P)3p$
C III	416.62	416.624	$1s^22s6p \rightarrow 1s^22p(^2P^\circ)4p$
N II	568.86	568.621	$2s^22p3s \rightarrow 2s^22p3p$
N II	589.78	589.725	$2s2p^2(^4P)3s \rightarrow 2s2p^2(^4P)3p$
N I	670.32	670.4839	$2s^22p^2(^3P)3p \rightarrow 2s^22p^2(^3P)4d$
N II	697.55	697.563	$2s^22p3d \rightarrow 2s^22p4p$
N II	713.82	713.885	$2s^22p3d \rightarrow 2s^22p4p$
N I	732.01	731.8975	$2s^22p^2(^3P)3p \rightarrow 2s^22p^2(^3P)4d$
N I	748.78	748.5178	$2s^22p^2(^3P)3p \rightarrow 2s^22p^2(^3P)4d$
C I	767.48	768.51859	$2s^22p3p \rightarrow 2s^22p5s$
N I	770.36	770.351	$2s^22p^2(^3P)4p \rightarrow 2s^22p^2(^1D)3d$
N I	792.43	791.5419	$2s^22p^2(^1D)3s \rightarrow 2s^22p^2(^1D)3p$

Table S5. The obtained gas composition (vol%) of plastic waste, battery separator waste, and silk waste with the CFMP.

Gas Species	Battery Separator Waste	Plastic Waste	Silk Waste
Hydrogen	43.30882	37.07398	40.67658
Carbon monoxide	11.88212	4.607007	35.42888
Carbon dioxide	15.7511	6.073512	18.82553
Methane	4.501022	14.89458	2.144618
Ethane	1.113465	1.446896	0.085508
Ethylene	8.860401	16.57897	0.828444
Dimethylmethane	0.792818	0.402366	0.050127
Propylene	7.097109	5.852195	0.21332
Acetylene	1.891893	1.948783	0.34637
1-Butene	0.56338	8.98748	0
2-methylpropene	1.815152	0.036823	0.015636
1,3-Butadiene	0.140719	0.051066	0.005481
Others	2.281995	2.046342	1.379507

Table S6. Model information.

Document Name and Reference	Treated As	Volumetric Properties
Boss-Extrude1	Solid Body	Mass:0.00965097 kg Volume:3.92699e-06 m^3 Density:2457.6 kg/m^3 Weight:0.0945795 N
Boss-Extrude1	Solid Body	Mass:0.0181593 kg Volume:7.38903e-06 m^3 Density:2457.6 kg/m^3 Weight:0.177961 N
Boss-Extrude1	Solid Body	Mass:0.000384 kg Volume:2e-06 m^3 Density:192 kg/m^3 Weight:0.0037632 N
Boss-Extrude1	Solid Body	Mass:7.8638e-06 kg Volume:8.83573e-09 m^3 Density:890 kg/m^3 Weight:7.70652e-05 N
Boss-Extrude1	Solid Body	Mass:0.0369663 kg Volume:0.000288799 m^3 Density:128 kg/m^3 Weight:0.36227 N
Boss-Extrude1	Solid Body	Mass:0.00965097 kg Volume:3.92699e-06 m^3 Density:2457.6 kg/m^3 Weight:0.0945795 N
Boss-Extrude1 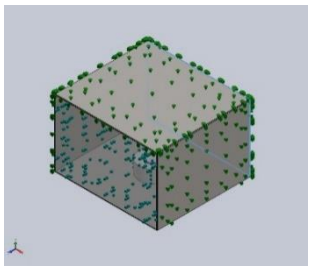	Solid Body	Mass:2.25225 kg Volume:0.00028875 m^3 Density:7800 kg/m^3 Weight:22.0721 N

Boss-Extrude1 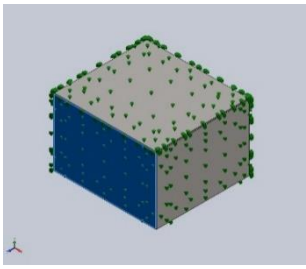	Solid Body	Mass:0.473088 kg Volume:0.0001925 m^3 Density:2457.6 kg/m^3 Weight:4.63626 N
Boss-Extrude1 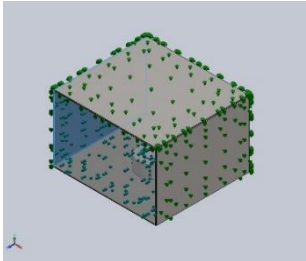	Solid Body	Mass:2.0475 kg Volume:0.0002625 m^3 Density:7800 kg/m^3 Weight:20.0655 N
Boss-Extrude1 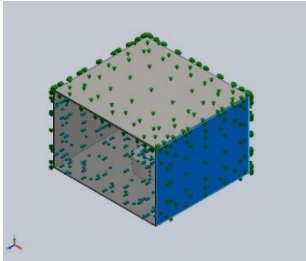	Solid Body	Mass:2.0475 kg Volume:0.0002625 m^3 Density:7800 kg/m^3 Weight:20.0655 N
Boss-Extrude1 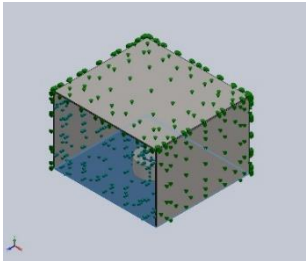	Solid Body	Mass:3.15315 kg Volume:0.00040425 m^3 Density:7800 kg/m^3 Weight:30.9009 N
Boss-Extrude1 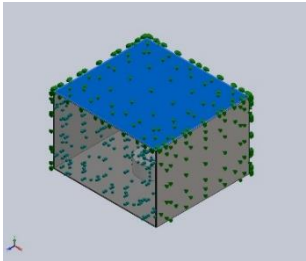	Solid Body	Mass:3.15315 kg Volume:0.00040425 m^3 Density:7800 kg/m^3 Weight:30.9009 N

Table S7. Study properties.

Study name	Thermal SteadyState
Analysis type	Thermal(Steady state)
Mesh type	Solid Mesh
Solver type	FFEPlus
Solution type	Steady state
Contact resistance defined?	No

Table S8. Material properties.

Model Reference	Properties	
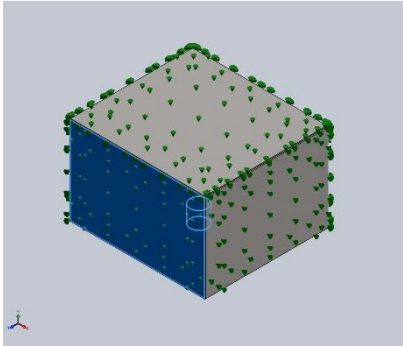	Name:	Glass
	Model type:	Linear Elastic Isotropic
	Thermal conductivity:	0.74976 W m^{-1} K^{-1}
	Specific heat:	834.61 J kg^{-1} K^{-1}
	Mass density:	2457.6 kg m^{-3}
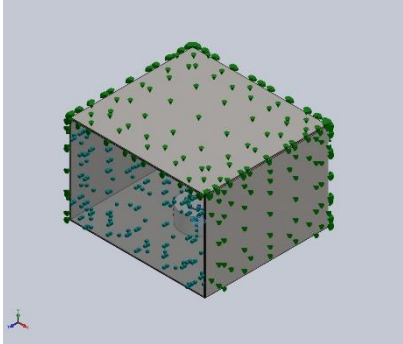	Name:	CarbonFoam
	Model type:	Linear Elastic Isotropic
	Thermal conductivity:	0.1 W m^{-1} K^{-1}
	Specific heat:	1200 J kg^{-1} K^{-1}
	Mass density:	192 kg m^{-3}
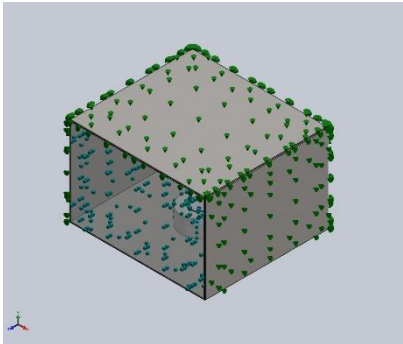	Name:	PP Copolymer
	Model type:	Linear Elastic Isotropic
	Thermal conductivity:	0.147 W m^{-1} K^{-1}
	Specific heat:	1881 J kg^{-1} K^{-1}
	Mass density:	890 kg m^{-3}
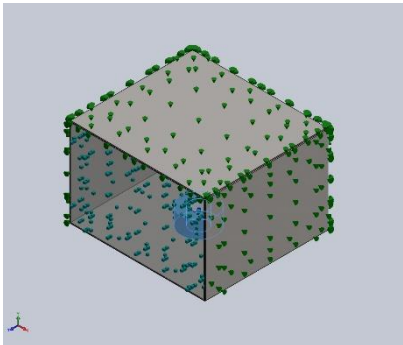	Name:	FiberFax
	Model type:	Linear Elastic Isotropic
	Thermal conductivity:	0.22 W m^{-1} K^{-1}
	Specific heat:	1140 J kg^{-1} K^{-1}
	Mass density:	128 kg m^{-3}

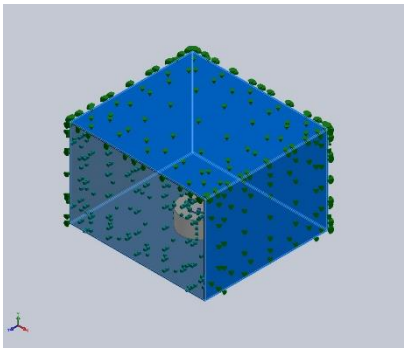

Name:	Plain Carbon Steel
Model type:	Linear Elastic Isotropic
Thermal conductivity:	43 W m^{-1} K^{-1}
Specific heat:	440 J kg^{-1} K^{-1}
Mass density:	7800 kg m^{-3}

Table S9. Thermal loads.

Load Name	Load Image	Load Details	
Convection-1	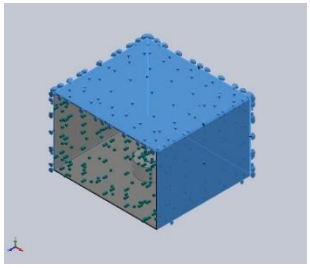	Entities:	16 face(s)
		Convection Coefficient:	10 W (m^{-2} K^{-1})
		Time variation:	Off
		Temperature variation:	Off
		Bulk Ambient Temperature:	300 K
		Time variation:	Off
Radiation-1	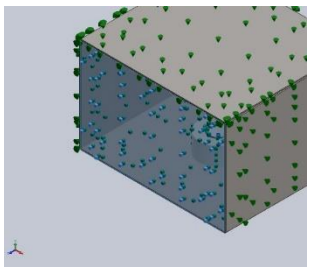	Entities:	1 face(s)
		Radiation Type:	Surface to ambient
		Ambient Temperature:	300 K
		Emissivity:	1
		View Factor:	1
Radiation-2	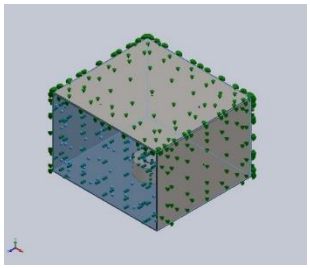	Entities:	5 face(s)
		Radiation Type:	Surface to surface
		Open system:	Off
		Emissivity:	0.4
Radiation-3	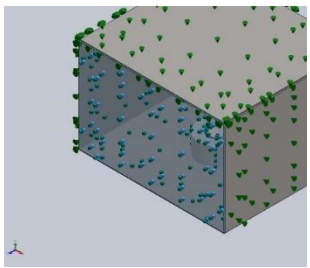	Entities:	1 face(s)
		Radiation Type:	Surface to surface
		Open system:	Off
		Emissivity:	1
Radiation-4	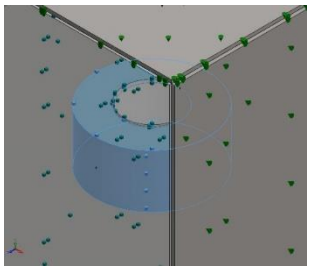	Entities:	2 face(s)
		Radiation Type:	Surface to surface
		Open system:	Off
		Emissivity:	0.6

Radiation-5	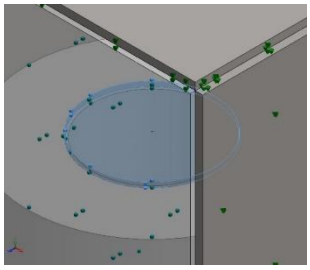	Entities: Radiation Type: Open system: Emissivity:	2 face(s) Surface to surface Off 0.95
Radiation-6	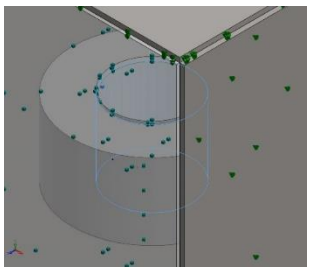	Entities: Radiation Type: Open system: Emissivity:	2 face(s) Surface to surface Off 0.95
Radiation-7	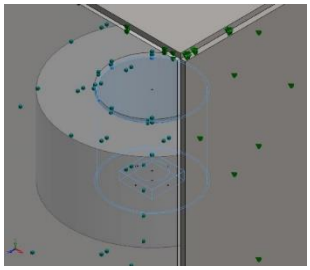	Entities: Radiation Type: Open system: Emissivity:	9 face(s) Surface to surface Off 1
Temperature-1	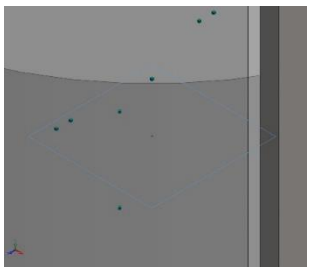	Entities: Temperature:	1 face(s) 3000 K
Radiation-8	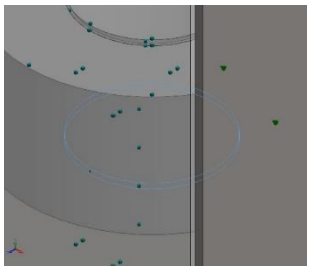	Entities: Radiation Type: Open system: Emissivity:	1 face(s) Surface to surface Off 0.95

Table S10. Contact information.

Contact	Contact Image	Contact Properties	
Global Contact	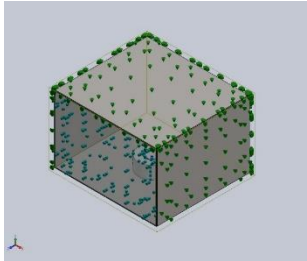	Type: Components: Options:	Bonded 1 component(s) Compatible mesh

Table S11. Mesh information.

Mesh type	Solid Mesh
Mesher Used:	Standard mesh
Automatic Transition:	Off
Include Mesh Auto Loops:	On
Jacobian points	4 Points
Element Size	14.9067 mm
Tolerance	0.384 mm
Mesh Quality Plot	High
Remesh failed parts with incompatible mesh	Off
Total Nodes	53778
Total Elements	29472
Maximum Aspect Ratio	1492.5
% of elements with Aspect Ratio < 3	8.19
% of elements with Aspect Ratio > 10	18.2
% of distorted elements(Jacobian)	0
Time to complete mesh(hh;mm;ss):	00:00:13

Table S12. Mesh control information.

Mesh Control Name	Mesh Control Image	Mesh Control Details	
Control-1	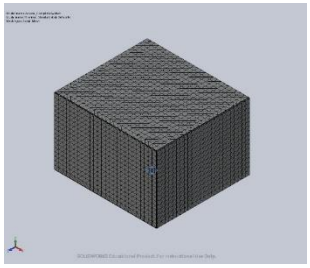	Entities: Units: Size: Ratio:	5 face(s) mm 2 1.5

Table S13. Decomposition temperatures of various organic proteins and PTFE. All concentrations are in weight percent. *From this work.

Material	Decomposition Temperature	Decomposition Products	Ref
PTFE	~400-650 °C	CF_2, HF, CF_4, COF_2, C_6H_6	39
Keratin	287-400 °C	C_6H_6O, C_7H_8O, Sulfides, Thiols, Nitriles	40
Collagen	300-420 °C	$C_2H_5NO_3$, $C_6H_5CH_3$, $C_6H_4(CH_3)_2$, C_6H_5-C_2H_6, C_5H_7N, C_7H_{12}, C_6H_6, SO_2, and more	41, 42
Fibroin	300-400 °C	H_2, CO, CH_4, C_2H_4*	43
Sericin	220-400 °C	H_2, CO, CH_4, C_2H_4*	43

What **Table S13** shows is that similar success should be expected in recycling PTFE, keratin, and collagen-based materials, due to their similar decomposition temperatures.

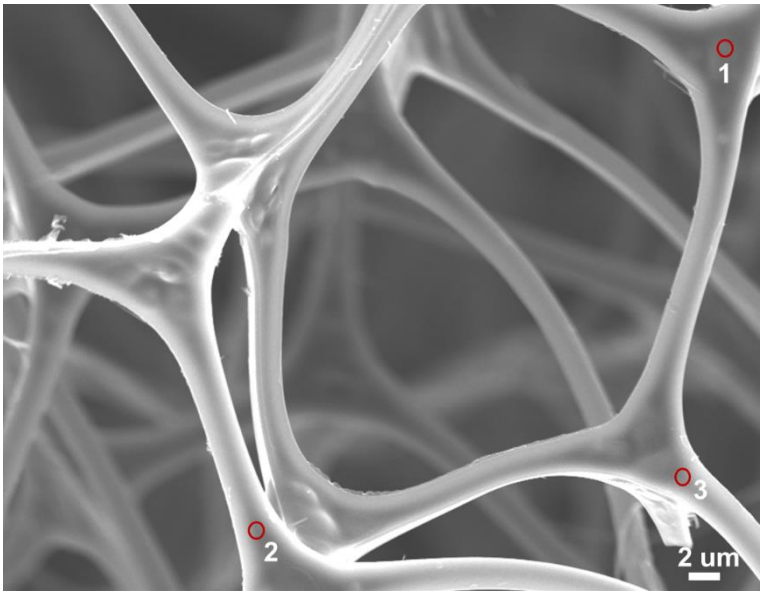

Figure S22. SEM image of carbon foam.

Table S14. Composition of carbon foam in Figure S22. The amounts of C, N, O (wt. %) are estimated from energy dispersive spectrometry (EDS).

Spots	C	N	O
1	62.47	26.38	11.15
2	77.01	15.08	7.91
3	71.91	20.68	7.41

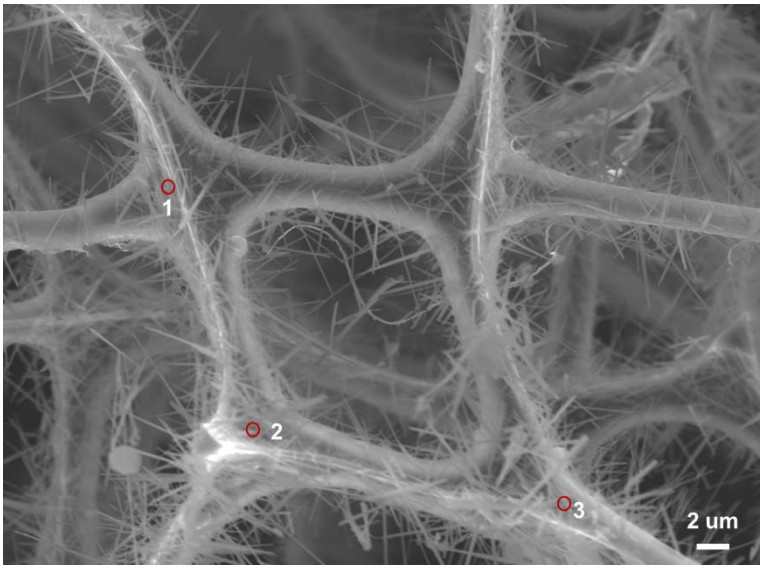

Figure S23. SEM image of carbon foam with batteries separator waste after 330 W and 8s.

Table S15. Composition of carbon foam with batteries separator waste after 330 W and 8s in Figure S23. The amounts of C, N, O (wt. %) are estimated from EDS.

Spots	C	N	O
1	44.52	17.97	37.52
2	47.02	25.19	27.79
3	45.03	23.96	31.01

The average nitrogen content of carbon foam was increased from 20.71% ± 4.61% (Table S14) to 22.37% ± 3.15% (Table S15) after the CFMP process by EDS. However, after testing the mean shift using a Student's T-test, a t-statistic of 0.42, and p-value of 0.696 was calculated, indicating that no significant change in nitrogen content within the foam occurred.

References

(1) Eriksen, M.; Mason, S.; Wilson, S.; Box, C.; Zellers, A.; Edwards, W.; Farley, H.; Amato, S. Microplastic pollution in the surface waters of the Laurentian Great Lakes. *Mar. Pollut. Bull.* **2013,** *77*, 177-182.

(2) Free, C. M.; Jensen, O. P.; Mason, S. A.; Eriksen, M.; Williamson, N. J.; Boldgiv, B. High-levels of microplastic pollution in a large, remote, mountain lake. *Mar. Pollut. Bull.* **2014,** *85*, 156-163.

(3) Dris, R.; Gasperi, J.; Rocher, V.; Saad, M.; Renault, N.; Tassin, B. Microplastic contamination in an urban area: a case study in Greater Paris. *Environ. Chem.* **2015,** *12*, 592-599.

(4) Lechner, A.; Keckeis, H.; Lumesberger-Loisl, F.; Zens, B.; Krusch, R.; Tritthart, M.; Glas, M.; Schludermann, E. The Danube so colourful: a potpourri of plastic litter outnumbers fish larvae in Europe's second largest river. *Environ. Pollut.* **2014,** *188*, 177-181.

(5) McCormick, A.; Hoellein, T. J.; Mason, S. A.; Schluep, J.; Kelly, J. J. Microplastic is an abundant and distinct microbial habitat in an urban river. *Environ. Sci. Technol.* **2014,** *48*, 11863-11871.

(6) Yonkos, L. T.; Friedel, E. A.; Perez-Reyes, A. C.; Ghosal, S.; Arthur, C. D. Microplastics in four estuarine rivers in the chesapeake bay, U.S.A. *Environ. Sci. Technol.* **2014,** *48*, 14195-14202.

(7) Fischer, E. K.; Paglialonga, L.; Czech, E.; Tamminga, M. Microplastic pollution in lakes and lake shoreline sediments–a case study on Lake Bolsena and Lake Chiusi (central Italy). *Environ. Pollut.* **2016,** *213*, 648-657.

(8) Anderson, P. J.; Warrack, S.; Langen, V.; Challis, J. K.; Hanson, M. L.; Rennie, M. D. Microplastic contamination in lake Winnipeg, Canada. *Environ. Pollut.* **2017,** *225*, 223-231.

(9) Xiong, X.; Zhang, K.; Chen, X.; Shi, H.; Luo, Z.; Wu, C. Sources and distribution of microplastics in China's largest inland lake–Qinghai Lake. *Environ. Pollut.* **2018,** *235*, 899-906.

(10) Uurasjärvi, E.; Hartikainen, S.; Setälä, O.; Lehtiniemi, M.; Koistinen, A. Microplastic concentrations, size distribution, and polymer types in the surface waters of a northern European lake. *Water Environ. Res.* **2020,** *92*, 149-156.

(11) Lima, A.; Costa, M.; Barletta, M. Distribution patterns of microplastics within the plankton of a tropical estuary. *Environ. Res.* **2014,** *132*, 146-155.

(12) Nan, B.; Su, L.; Kellar, C.; Craig, N. J.; Keough, M. J.; Pettigrove, V. Identification of microplastics in surface water and Australian freshwater shrimp Paratya australiensis in Victoria, Australia. *Environ. Pollut.* **2020,** *259*, 113865.

(13) Nel, H.; Froneman, P. A quantitative analysis of microplastic pollution along the south-eastern coastline of South Africa. *Mar. Pollut. Bull.* **2015,** *101*, 274-279.

(14) Lahens, L.; Strady, E.; Kieu-Le, T. C.; Dris, R.; Boukerma, K.; Rinnert, E.; Gasperi, J.; Tassin, B. Macroplastic and microplastic contamination assessment of a tropical river (Saigon River, Vietnam) transversed by a developing megacity. *Environ. Pollut.* **2018,** *236*, 661-671.

(15) de Carvalho, D. G.; Neto, J. A. B. Microplastic pollution of the beaches of

Guanabara Bay, Southeast Brazil. *Ocean Coast. Manage.* **2016,** *128*, 10-17.
(16) Gewert, B.; Ogonowski, M.; Barth, A.; MacLeod, M. Abundance and composition of near surface microplastics and plastic debris in the Stockholm Archipelago, Baltic Sea. *Mar. Pollut. Bull.* **2017,** *120*, 292-302.
(17) Tang, G.; Liu, M.; Zhou, Q.; He, H.; Chen, K.; Zhang, H.; Hu, J.; Huang, Q.; Luo, Y.; Ke, H.; Chen, B.; Xu, X.; Cai, M. Microplastics and polycyclic aromatic hydrocarbons (PAHs) in Xiamen coastal areas: Implications for anthropogenic impacts. *Sci. Total Environ.* **2018,** *634*, 811-820.
(18) Nel, H. A.; Hean, J. W.; Noundou, X. S.; Froneman, P. W. Do microplastic loads reflect the population demographics along the southern African coastline? *Mar. Pollut. Bull.* **2017,** *115*, 115-119.
(19) Desforges, J. P. W.; Galbraith, M.; Dangerfield, N.; Ross, P. S. Widespread distribution of microplastics in subsurface seawater in the NE Pacific Ocean. *Mar. Pollut. Bull.* **2014,** *79*, 94-99.
(20) Peters, W. Microplastic fibres in Pacific sand lance (Ammodytes personatus) burying habitats in the Strait of Georgia, British Columbia, Canada. **2018**.
(21) Isobe, A.; Kubo, K.; Tamura, Y.; Kako, S. i.; Nakashima, E.; Fujii, N. Selective transport of microplastics and mesoplastics by drifting in coastal waters. *Mar. Pollut. Bull.* **2014,** *89*, 324-330.
(22) Lusher, A. L.; Tirelli, V.; O'Connor, I.; Officer, R. Microplastics in Arctic polar waters: the first reported values of particles in surface and sub-surface samples. *Sci. Rep.* **2015,** *5*, 14947.
(23) do Sul, J. A. I.; Costa, M. F.; Barletta, M.; Cysneiros, F. J. A. Pelagic microplastics around an archipelago of the Equatorial Atlantic. *Mar. Pollut. Bull.* **2013,** *75*, 305-309.
(24) Gilfillan, L. R.; Ohman, M. D.; Doyle, M. J.; Watson, W. Occurrence of plastic micro-debris in the southern California Current system. *Cal. Coop. Ocean. Fish.* **2009,** *50*, 123-133.
(25) Cole, M.; Webb, H.; Lindeque, P. K.; Fileman, E. S.; Halsband, C.; Galloway, T. S. Isolation of microplastics in biota-rich seawater samples and marine organisms. *Sci. Rep.* **2014,** *4*, 4528.
(26) Chae, D. H.; Kim, I. S.; Kim, S. K.; Song, Y. K.; Shim, W. J. Abundance and distribution characteristics of microplastics in surface seawaters of the Incheon/Kyeonggi coastal region. *Arch. Environ. Contam. Toxicol.* **2015,** *69*, 269-278.
(27) Song, Y. K.; Hong, S. H.; Jang, M.; Han, G. M.; Shim, W. J. Occurrence and distribution of microplastics in the sea surface microlayer in Jinhae Bay, South Korea. *Arch. Environ. Contam. Toxicol.* **2015,** *69*, 279-287.
(28) Panti, C.; Giannetti, M.; Baini, M.; Rubegni, F.; Minutoli, R.; Fossi, M. C. Occurrence, relative abundance and spatial distribution of microplastics and zooplankton NW of Sardinia in the Pelagos Sanctuary Protected Area, Mediterranean Sea. *Environ. Chem.* **2015,** *12*, 618-626.
(29) Mu, J.; Zhang, S.; Qu, L.; Jin, F.; Fang, C.; Ma, X.; Zhang, W.; Wang, J. Microplastics abundance and characteristics in surface waters from the Northwest Pacific, the Bering Sea, and the Chukchi Sea. *Mar. Pollut. Bull.* **2019,** *143*, 58-65.
(30) Isobe, A.; Uchiyama-Matsumoto, K.; Uchida, K.; Tokai, T. Microplastics in the

Southern Ocean. *Mar. Pollut. Bull.* **2017,** *114*, 623-626.
(31) Antunes, J.; Frias, J.; Sobral, P. Microplastics on the Portuguese coast. *Mar. Pollut. Bull.* **2018,** *131*, 294-302.
(32) Zhao, S.; Zhu, L.; Wang, T.; Li, D. Suspended microplastics in the surface water of the Yangtze Estuary System, China: first observations on occurrence, distribution. *Mar. Pollut. Bull.* **2014,** *86*, 562-568.
(33) Jie, X.; Li, W.; Slocombe, D.; Gao, Y.; Banerjee, I.; Gonzalez-Cortes, S.; Yao, B.; AlMegren, H.; Alshihri, S.; Dilworth, J.; Thomas, J.; Xiao, T.; Edwards, P. Microwave-initiated catalytic deconstruction of plastic waste into hydrogen and high-value carbons. *Nat. Catal.* **2020,** *3*, 902-912.
(34) Meeprasertsagool, P.; Watthanaphanit, A.; Ueno, T.; Saito, N.; Reubroycharoen, P. New insights into vegetable oil pyrolysis by cold plasma technique. *Energy Procedia* **2017,** *138*, 1153-1158.
(35) Domínguez, A.; Fidalgo, B.; Fernández, Y.; Pis, J. J.; Menéndez, J. A. Microwave-assisted catalytic decomposition of methane over activated carbon for CO2-free hydrogen production. *Int. J. Hydrog. Energy* **2007,** *32*, 4792-4799.
(36) Fidalgo, B.; Domínguez, A.; Pis, J. J.; Menéndez, J. A. Microwave-assisted dry reforming of methane. *Int. J. Hydrog. Energy* **2008,** *33*, 4337-4344.
(37) Jiang, H.; Liu, W.; Zhang, X.; Qiao, J. Chemical Recycling of Plastics by Microwave-Assisted High-Temperature Pyrolysis. *Glob. Chall.* **2020,** *4*, 1900074.
(38) Lam, S. S.; Wan Mahari, W. A.; Ma, N. L.; Azwar, E.; Kwon, E. E.; Peng, W.; Chong, C. T.; Liu, Z.; Park, Y.-K, Microwave pyrolysis valorization of used baby diaper. *Chemosphere* **2019,** *230*, 294-302.
(39) Conesa, J. A.; Font, R. Polytetrafluoroethylene decomposition in air and nitrogen. *Polym. Eng. Sci.* **2001,** *41*, 2137-2147.
(40) Brebu, M.; Spiridon, I. Thermal degradation of keratin waste. *J. Anal. Appl. Pyrolysis* **2011,** *91*, 288-295.
(41) Bozec, L.; Odlyha, M. Thermal denaturation studies of collagen by microthermal analysis and atomic force microscopy. *Biophys. J.* **2011,** *101*, 228-36.
(42) Yang, P.; He, X.; Zhang, W.; Qiao, Y.; Wang, F.; Tang, K. Study on thermal degradation of cattlehide collagen fibers by simultaneous TG–MS–FTIR. *J. Therm. Anal. Calorim.* **2017,** *127*, 2005-2012.
(43) Tsukada, M. Thermal decomposition behavior of sericin cocoon. *J. Appl. Polym. Sci.* **1978,** *22*, 543-554.